Journal of the Mechanics and Physics of Solids 124 (2019) 244–263

Contents lists available at ScienceDirect

Journal of the Mechanics and Physics of Solids

journal homepage: www.elsevier.com/locate/jmps

Mechanics of hard-magnetic soft materials

Ruike Zhao[a,b,1], Yoonho Kim[a,1], Shawn A. Chester[c], Pradeep Sharma[d,e], Xuanhe Zhao[a,f,*]

[a] Soft Active Materials Laboratory, Department of Mechanical Engineering, Massachusetts Institute of Technology, Cambridge, MA 02139, USA
[b] Department of Mechanical and Aerospace Engineering, The Ohio State University, Columbus, OH 43210, USA
[c] Department of Mechanical and Industrial Engineering, New Jersey Institute of Technology, Newark, NJ 07102, USA
[d] Department of Mechanical Engineering and The Materials Science and Engineering Program, University of Houston, TX 77004, USA
[e] Department of Physics, University of Houston, TX 77004, USA
[f] Department of Civil and Environmental Engineering, Massachusetts Institute of Technology, Cambridge, MA 02139, USA

ARTICLE INFO

Article history:
Received 4 September 2018
Revised 1 October 2018
Accepted 7 October 2018
Available online 10 October 2018

ABSTRACT

Soft materials that can undergo rapid and large deformation through the remote and wireless action of external stimuli offer a range of tantalizing applications such as soft robots, flexible electronics, and biomedical devices. A natural and simple embodiment of such materials is to embed magnetic particles in soft polymers. Unfortunately, existing magnetically responsive soft materials such as magnetorheological elastomers and ferrogels typically use magnetically-soft particles such as iron and iron oxides, which are characterized by the low coercivity and hence lack the capability to retain remnant magnetism. Accordingly, their deformation is limited to simple elongation or shortening, rendering these materials substantially unsuited for the complex transformations required in many applications. To introduce shape-programmability, magnetically-hard particles with high coercivity have been incorporated in mechanically soft materials. In addition, recent works aimed at ameliorating this situation have developed fabrication techniques and facile routes to engineer rapid and complex transformations in a programmable manner by introducing intricate patterns of magnetic polarities in soft materials. The resulting structures, when properly designed, have been shown to exhibit a diverse and rich array of actuation behavior. In this work, we develop a suitable theoretical framework to analyze these so-called hard-magnetic soft materials to facilitate the rational design of magnetically activated functional structures and devices based on a quantitative prediction of complex shape changes. We adopt a nonlinear field theory to describe the finite deformation coupled with magnetic fields and argue that the macroscopic behavior of the fabricated mate-

* Corresponding author at: Soft Active Materials Laboratory, Department of Mechanical Engineering, Massachusetts Institute of Technology, Cambridge, MA 02139, USA.
E-mail address: zhaox@mit.edu (X. Zhao).
[1] Both the authors contributed equally to the current work.

https://doi.org/10.1016/j.jmps.2018.10.008

rials requires a new constitutive classification — *ideal hard-magnetic soft material* — which assumes that (i) the material has a residual magnetic flux density, and (ii) the induced magnetic flux density exhibits a linear relation with the applied actuating magnetic field. We implement the theory and constitutive law in a finite-element framework and find remarkable agreement between the simulation and experimental results on various deformation modes of hard-magnetic soft materials. Using the developed (and validated) model, we present a set of illustrative examples to highlight the use of our model-based simulation to guide the design of experimentally realizable complex shape-morphing structures based on hard-magnetic soft materials.

1. Introduction

Magnetoactive soft materials such as magnetorheological elastomers and ferrogels are commonly composed of magnetic particles of iron or iron oxides embedded in polymeric matrices (Ginder et al., 1999; Li et al., 2014; Rigbi and Jilken, 1983; Jolly et al., 1996; Ginder, 1996). Under the influence of magnetic fields, the embedded particles interact with one another and with the polymer matrices to rapidly and dramatically deform while changing mechanical properties such as stiffness in a controlled manner (Ginder et al., 2002). The controlled variation of mechanical properties in magnetorheological elastomers has been used in applications such as vibration absorbers (Li et al., 2014; Ginder et al., 2001; Deng et al., 2006) and isolators (Opie and Yim, 2011; Liao et al., 2012), sensing devices (Li et al., 2009; Bica et al., 2014), and engine mounts (Ginder et al., 1999; Jeong et al., 2013; Kavlicoglu et al., 2011). The controlled deformation of magnetoactive soft materials has been exploited in applications such as soft actuators (Kashima et al., 2012; Böse et al., 2012; Nguyen and Ramanujan, 2010), magnetically activated pumps (Hong et al., 2014), and active scaffolds for drug and cell delivery (Zhao et al., 2011; Cezar et al., 2014). The aforementioned magnetoactive materials are typically based on embedding particles of low-coercivity ferromagnetic materials, or soft-magnetic materials, such as iron and iron oxides (Rigbi and Jilken, 1983; Zrínyi et al., 1996; Borcea and Bruno, 2001). These soft-magnetic materials can develop strong magnetization along the applied magnetic field, however due the their low coercivity (i.e. low $\mathbf{H}^{\mathrm{c}}$ in Fig. 1), they do not adequately retain the strong magnetism once the external field has been removed (Ginder et al., 1999; Danas et al., 2012; Bertotti, 1998; Harne et al., 2018; Evans et al., 2012). Hence, the controlled deformation of these materials is essentially limited to simple elongation or compression under an externally applied magnetic field (Zrínyi et al., 1996; Evans et al., 2007).

Recently, particles of high-coercivity ferromagnetic materials, or hard-magnetic materials, such as neodymium-iron-boron (NdFeB) have been embedded in soft materials for programmable and/or complex shape changes (Lum et al., 2016; Hu et al., 2018; Kim et al., 2018). The high remnant characteristics of hard-magnetic materials allow them to retain high residual magnetic flux density (i.e. high $\mathbf{B}^{\mathrm{r}}$) even in the absence of magnetic fields once they are magnetically saturated (Fig. 1). In addition, the high coercivity (i.e. high $\mathbf{H}^{\mathrm{c}}$) of hard-magnetic materials helps them sustain the high residual magnetic flux density over a wide range of applied magnetic fields below the coercive field strength. The recent development of a fabrication technique to program intricate patterns of magnetic polarities in 3D-printed soft materials (Kim et al., 2018), as depicted in Fig. 2, has enabled the use of such hard-magnetic materials to create complex modes of transformation. Application of external magnetic fields induces torques on the embedded hard-magnetic particles in the programmed domains, and these magnetic torques create internal stresses that collectively lead to a macroscale response in the form of complex shape changes. Such rapid and complex transformation of 3D-printed hard-magnetic soft materials appear to pave the way for new applications in soft robotics, flexible electronics, and biomedical devices (Kim et al., 2018).

The material described in the preceding paragraph appears to exhibit an emergent response that is consistent with magnetically hard materials (e.g. NdFeB magnets) but is mechanically very soft. We name such a material, “hard-magnetic soft material”. To better understand the behavior of these so-called hard-magnetic soft materials and hence quantitatively predict the complex transformation upon actuation, a theoretical model and its computational implementation are required. Moreover, such capability of accurately predicting the final shape under the influence of magnetic interaction is crucial to guide the design of new functional structures and devices based on the programmed shape changes (Fig. 2).

There is rather long and checkered history underlying the modeling of mechanics of multifunctional materials. For the sake of brevity, we avoid a detailed review of the literature and only point to the works that are most germane to the central theme of our paper. In the context of magnetically responsive materials, several works have discussed the microscale and macroscale behavior of conventional magnetorheological elastomers and ferrogels in which soft-magnetic materials are embedded (Borcea and Bruno, 2001; Danas et al., 2012; Dorfmann and Ogden, 2003; Dorfmann and Ogden, 2016; Galipeau and Castañeda, 2013; Kankanala and Triantafyllidis, 2004; Castañeda and Galipeau, 2011). For example, Tiersten (1965), Brown (1966), and Dorfmann and Ogden (2003, 2016) considered the magnetoactive soft material as a homogenized continuum body with a constitutive law given by a Helmholtz free energy as a function of field variables such as deformation gradient and magnetic field or Cauchy–Green tensor and magnetic moment density. Danas et al. (2012) and Kankanala and Triantafyllidis (2004) validated these existing models with experimental data such as the uniaxial loading, shear, and magnetostriction of magnetoactive soft materials in the presence of applied magnetic fields. To consider interparticle interactions in such ho-

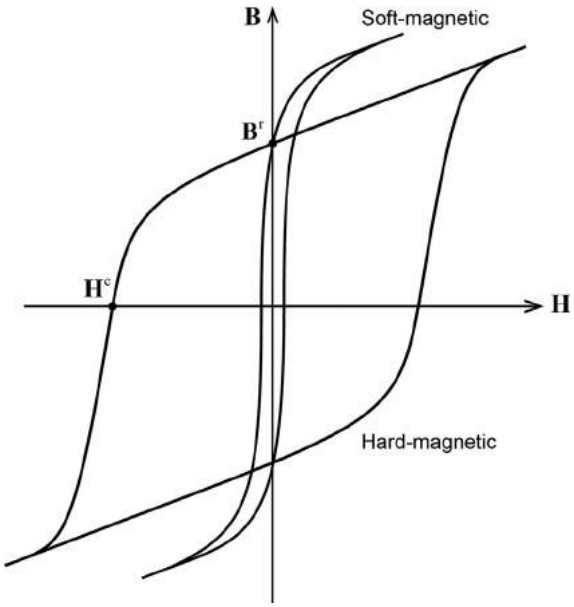

Fig. 1. Magnetic hysteresis loops and **B-H** curves of soft-magnetic and hard-magnetic materials, both of which are ferromagnetic and thus develop strong magnetic flux density **B** when exposed to an external magnetic field **H**. Soft-magnetic materials, or low-coercivity ferromagnetic materials, form a sharp and narrow **B-H** curve due to the low coercive field $\mathbf{H}^c$ and hence do not sustain high residual magnetic flux density $\mathbf{B}^r$ independently of external fields. Hard-magnetic materials possess much higher coercivity and thus can retain high residual magnetic flux density $\mathbf{B}^r$ unless a strong demagnetizing field beyond the coercivity $\mathbf{H}^c$ is applied.

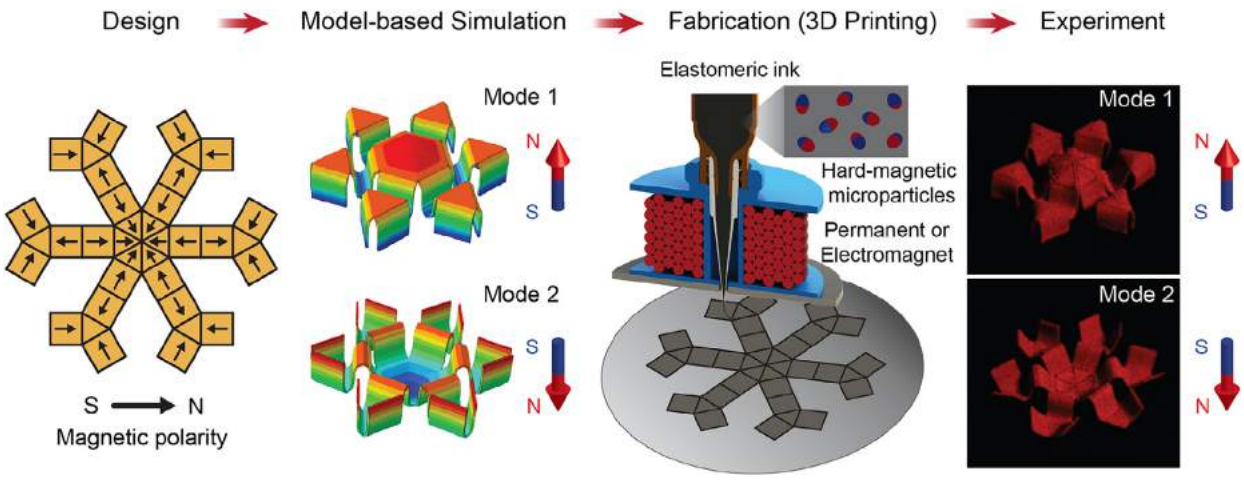

Fig. 2. Model-guided design and fabrication of complex shape-morphing structures based on programming intricate patterns of ferromagnetic domains in 3D-printed hard-magnetic soft materials (adapted and modified from (Kim et al., 2018)).

mogenized continuum models, Borcea and Bruno (2001), Yin et al. (2006), Galipeau and Castañeda (2013) and Castañeda and Galipeau (2011) considered the microstructure and the distribution of magnetic particles embedded in polymeric matrices. Finally, a recent comprehensive exposition by Liu (2014) compares various approaches to the theoretical development of continuum electromagnetism of deformable continua.

The existing models for magnetoactive soft materials are largely focused on magnetorheological elastomers or ferrogels and are not readily applicable to the new class of developed materials — hard-magnetic soft materials with programmed magnetic domains. In particular, given the recent advances in fabrication techniques for shape-programmable magnetic soft materials (Lum et al., 2016; Hu et al., 2018; Kim et al., 2018), a systematic theoretical framework, constitutive law development, and computational approach for hard-magnetic soft materials are warranted. In this paper, we develop a *simple*[1]

[1] The rigorous development of a field theory for the complex media we have undertaken to study is characterized by several subtleties. We emphasize the word "simple" here to signify that our main objective is to create a framework that is readily *usable*, *consistent* with experiments, and yet espouses the central tents of continuum mechanics.

nonlinear field theory to describe the coupling of finite deformation and magnetic fields to model such hard-magnetic soft materials. We propose a specific form for the constitutive law named *ideal hard-magnetic soft material*, which assumes that (i) the material has a residual magnetic flux density, and (ii) the induced magnetic flux density is linearly related to the applied magnetic field over a wide range of field strength required for actuation.

The developed theoretical model accounts for the mechanical effects induced by applied magnetic fields using magnetic Cauchy stresses (Danas et al., 2012; Dorfmann and Ogden, 2003, 2016; Kankanala and Triantafyllidis, 2004; Kovetz, 2000), instead of magnetic body forces (Yih-Hsing and Chau-Shioung, 1973; Pao, 1978). Magnetic body torques generated by the embedded magnetized particles under externally applied magnetic fields cause the magnetic Cauchy stress to be asymmetric. Correspondingly, the *total* Cauchy stress that accounts for both the magnetic and mechanical stress components in hard-magnetic soft materials can also be asymmetric. We implement the developed theoretical model within a finite-element environment in the form of an Abaqus/Standard user-element subroutine and validate the model through a set of experiments on various modes of magnetically induced deformations of hard-magnetic soft materials.

The outline of this paper is as follows. In Section 2, we summarize the basic equations of the nonlinear field theory for large deformation induced by magneto-elastic field coupling in soft materials. Section 3 provides a framework to formulate the constitutive law for hard-magnetic soft materials and a specific constitutive model for the ideal hard-magnetic soft material. In Section 4**,** we present the numerical implementation of the ideal hard-magnetic soft material into a commercial finite-element software while we validate our constitutive law and computational model in Section 5 through a set of experiments. We further validate the developed model in Section 6 by comparing the model-based simulation and the experimental results for complex shape changes of 3D-printed hard-magnetic soft materials. We conclude in Section 7 where we also speculate regarding the potential future use of the developed framework.

2. Nonlinear field theory

2.1. Kinematics

Consider a deformable solid continuum body in the reference (i.e. undeformed) state with material particles labeled by their position vectors $\mathbf{X}$. The deformable solid body can span the whole space. In the current (i.e. deformed) state, in which the current body is denoted as B_t, the material particle $\mathbf{X}$ occupies the position dictated by a smooth deformation map: $\mathbf{x} = \chi(\mathbf{X})$. The deformation gradient tensor $\mathbf{F}$ is defined by

$$\mathbf{F} = \mathrm{Grad}\ \chi, \tag{2.1}$$

where Grad denotes the gradient operator with respect to $\mathbf{X}$. In what follows, upper case letters will be used to denote the differential operators with respect to the reference coordinate $\mathbf{X}$ (e.g. Grad, Div) whereas, correspondingly, lower case will be used for the same operators in the current configuration. As conventional, we further denote by $J = \det\mathbf{F}$, the deformation Jacobian.

The Cauchy stress tensor (or true stress tensor) and the first Piola–Kirchhoff stress tensor (or nominal stress tensor) are denoted as $\boldsymbol{\sigma}$ and $\mathbf{P}$, respectively, which are related by

$$\boldsymbol{\sigma} = J^{-1}\mathbf{P}\mathbf{F}^{\mathrm{T}} \quad \text{or} \quad \mathbf{P} = J\boldsymbol{\sigma}\mathbf{F}^{-\mathrm{T}}. \tag{2.2}$$

We denote the magnetic field vector and the magnetic flux density vector in the current configuration of the considered material as $\mathbf{H}$ and $\mathbf{B}$, respectively. Correspondingly, the nominal magnetic field vector and the magnetic flux density vector in the reference configuration are denoted by $\tilde{\mathbf{H}}$ and $\tilde{\mathbf{B}}$, respectively. Standard kinematics can be used to express the relation between $\mathbf{H}$ and $\tilde{\mathbf{H}}$ as

$$\mathbf{H} = \mathbf{F}^{-\mathrm{T}}\tilde{\mathbf{H}} \quad \text{or} \quad \tilde{\mathbf{H}} = \mathbf{F}^{\mathrm{T}}\mathbf{H}, \tag{2.3}$$

and the relation between $\mathbf{B}$ and $\tilde{\mathbf{B}}$ as

$$\mathbf{B} = J^{-1}\mathbf{F}\tilde{\mathbf{B}} \quad \text{or} \quad \tilde{\mathbf{B}} = J\mathbf{F}^{-1}\mathbf{B}. \tag{2.4}$$

2.2. Mass conservation, equilibrium conditions, and Maxwell's equations

The conservation of mass for the continuum material under static conditions requires

$$\rho = J^{-1}\tilde{\rho} \quad \text{or} \quad \tilde{\rho} = \rho J, \tag{2.5}$$

where ρ is the mass density of the material in the current configuration, and $\tilde{\rho}$ is the nominal mass density of the material in the reference configuration.

Assuming quasi-static conditions with the acceleration of all material particles being zero, the following equation must be satisfied in the current configuration for the material to be in equilibrium:

$$\mathrm{div}\,\boldsymbol{\sigma} + \mathbf{f} = \mathbf{0}, \tag{2.6}$$

where, as per our stated convention, div$\boldsymbol{\sigma}$ denotes the divergence of $\boldsymbol{\sigma}$ with respect to $\mathbf{x}$, and $\mathbf{f}$ denotes the body force per unit volume in the current configuration. Correspondingly, the equilibrium equation in the reference configuration can be written as

$$\text{Div}\,\mathbf{P}+\tilde{\mathbf{f}}=\mathbf{0}, \tag{2.7}$$

where $\tilde{\mathbf{f}}$ denotes the body force per unit volume in the reference configuration. We note here that the body force shown in the above equations are considered to originate from non-magnetic sources (e.g. gravity) and not magnetic fields. The effect of magnetic fields has been accounted for in the stress tensors (Dorfmann and Ogden, 2003, 2016; Pao, 1978). The relation between the referential and the spatial body forces in the two configurations is given as

$$\mathbf{f}=J^{-1}\tilde{\mathbf{f}} \quad \text{or} \quad \tilde{\mathbf{f}}=J\mathbf{f}. \tag{2.8}$$

We remark here that the stress tensors defined in Eqs. (2.2) and (2.7) are the total stresses, or the physical stresses that an element in the body will experience. These stresses account for both the stress caused by pure mechanical deformation (if the magnetic field were to be absent) and the stress induced by magnetic fields. As we will elaborate further in due course, the part of the total stress due to magnetic fields may be asymmetric, and consequently, the total Cauchy stress may also be asymmetric. As well-known, asymmetric stresses can arise in a classical continua in the presence of external body torques such as due to magnetic fields. This is to be distinguished from a non-classical continua such as micropolar, Cosserat, and others which may admit asymmetric stresses due to the accounting of higher order effects attributed to gradients of rotation and strain or the presence of so-called internal micro-rotations (Truesdell and Toupin, 1960; Malvern, 1969; Fung, 1994; Holzapfel, 2000; McMeeking and Landis, 2004; Lai et al., 2009)[2]. Since angular momentum must be conserved to ensure equilibrium, the asymmetric part of the total Cauchy stress must satisfy a suitable balance law as follows:

$$\boldsymbol{\varepsilon}:\mathbf{S}+\mathbf{m}=0, \tag{2.9}$$

where $\boldsymbol{\varepsilon}$ is the third-order permutation tensor, $\mathbf{S}=(\boldsymbol{\sigma}-\boldsymbol{\sigma}^{\mathrm{T}})/2$ is the asymmetric (or skew) part of the total Cauchy stress tensor, the operator : denotes the double contraction of two tensors, and $\mathbf{m}$ denotes the body torque generated by the magnetized domain under the action of an external magnetic field. Eq. (2.9) can also be expressed in the following indicial form: $\varepsilon_{ijk}S_{ij}+m_k=0$.

In the absence of any free current and time-variation of the pertinent electromagnetic quantities, the static Maxwell's equations in the current configuration are:

$$\text{div}\,\mathbf{B}=0, \tag{2.10a}$$

$$\text{curl}\,\mathbf{H}=\mathbf{0}, \tag{2.10b}$$

Correspondingly, the Maxwell's equations in the reference configuration are:

$$\text{Div}\,\tilde{\mathbf{B}}=0, \tag{2.11a}$$

$$\text{Curl}\,\tilde{\mathbf{H}}=\mathbf{0}. \tag{2.11b}$$

2.3. Boundary conditions

In the absence of applied tractions, the mechanical boundary condition in the current configuration across a surface or interface can be expressed as

$$[\boldsymbol{\sigma}]\mathbf{n}=\mathbf{0}, \tag{2.12}$$

where $[\cdot]$ denotes the jump in the relevant field, and $\mathbf{n}$ is the outward unit normal to the surface in the current configuration. Correspondingly, the mechanical boundary condition in the reference configuration can be expressed as

$$[\mathbf{P}]\mathbf{N}=\mathbf{0}, \tag{2.13}$$

where $\mathbf{N}$ is the outward unit normal to the surface in the reference configuration. If any part of the boundary is constrained kinematically, the mechanical boundary condition on that part of the boundary is prescribed by specifying $\mathbf{x}=\chi(\mathbf{X})$. Similarly, the magnetic boundary conditions in the current configuration can be expressed as

$$\mathbf{n}\cdot[\mathbf{B}]=0, \tag{2.14a}$$

$$\mathbf{n}\times[\mathbf{H}]=\mathbf{0}. \tag{2.14b}$$

[2] In these non-classical continua, in which often the stress is indeed asymmetric, there is also a presence of size-effects due to introduction of a characteristic material length scale. We will revisit this topic in the concluding remarks when we discuss future work.

Correspondingly, the magnetic boundary conditions in the reference configuration are:

$$\mathbf{N}\cdot[\tilde{\mathbf{B}}]=0, \tag{2.15a}$$

$$\mathbf{N}\times[\tilde{\mathbf{H}}]=\mathbf{0}. \tag{2.15b}$$

3. Constitutive model

The uniqueness of the macroscopic response of the hard-magnetic soft materials requires a careful specification of a suitable constitutive law that is capable of capturing the observed macroscopic behavior in experiments. In this section, we proceed to outline the various physical considerations underpinning the development of this constitutive law.

3.1. Residual magnetic flux density

Hard-magnetic materials can retain high remnant magnetization (remanence) and hence high residual magnetic flux density even in the absence of applied magnetic fields once they are magnetically saturated (Fig. 1). The high coercivity of hard-magnetic materials further helps them sustain the high residual magnetic flux density $\mathbf{B}^{\mathrm{r}}$ over a wide range of applied magnetic fields below the coercive field strength $\mathbf{H}^{\mathrm{c}}$ (Fig. 1). The residual magnetic flux density in a hard-magnetic soft material is defined in the current configuration as

$$\mathbf{B}^{\mathrm{r}}=\mathbf{B}|_{\mathbf{H}=\mathbf{0}}. \tag{3.1}$$

Correspondingly, the nominal residual magnetic flux density in the reference configuration is defined as

$$\tilde{\mathbf{B}}^{\mathrm{r}}=\tilde{\mathbf{B}}|_{\tilde{\mathbf{H}}=\mathbf{0}}. \tag{3.2}$$

According to Eq. (2.4), the relation between $\mathbf{B}^{\mathrm{r}}$ and $\tilde{\mathbf{B}}^{\mathrm{r}}$ can be expressed as

$$\mathbf{B}^{\mathrm{r}}=J^{-1}\mathbf{F}\tilde{\mathbf{B}}^{\mathrm{r}}\quad\text{or}\quad\tilde{\mathbf{B}}^{\mathrm{r}}=J\mathbf{F}^{-1}\mathbf{B}^{\mathrm{r}}. \tag{3.3}$$

3.2. General form of the constitutive model

Following the standard convention in nonlinear elasticity and thermodynamics, we develop a constitutive model for hard-magnetic soft materials based on the nominal Helmholtz free energy function $\tilde{W}$, which denotes the Helmholtz free energy per unit reference volume (Dorfmann and Ogden, 2003; McMeeking and Landis, 2004; Ogden, 1972; Suo et al., 2008). The nominal Helmholtz free energy density $\tilde{W}$ is regarded as a function of two independent variables $\mathbf{F}$ and $\tilde{\mathbf{B}}$ with one state parameter $\tilde{\mathbf{B}}^{\mathrm{r}}$, i.e. $\tilde{W}(\mathbf{F},\tilde{\mathbf{B}})$. By work conjugation, we can state that:

$$\mathbf{P}=\frac{\partial\tilde{W}(\mathbf{F},\tilde{\mathbf{B}})}{\partial\mathbf{F}}, \tag{3.4a}$$

$$\tilde{\mathbf{H}}=\frac{\partial\tilde{W}(\mathbf{F},\tilde{\mathbf{B}})}{\partial\tilde{\mathbf{B}}}. \tag{3.4b}$$

By substituting Eq. (3.4) into Eqs. (2.2) and (2.3), we have

$$\boldsymbol{\sigma}=\frac{1}{J}\frac{\partial\tilde{W}(\mathbf{F},\tilde{\mathbf{B}})}{\partial\mathbf{F}}\mathbf{F}^{\mathrm{T}}, \tag{3.5a}$$

$$\mathbf{H}=\mathbf{F}^{-\mathrm{T}}\frac{\partial\tilde{W}(\mathbf{F},\tilde{\mathbf{B}})}{\partial\tilde{\mathbf{B}}}. \tag{3.5b}$$

3.3. Ideal hard-magnetic soft material

To facilitate physical interpretation and separation of the magneto-mechanical constitutive laws, we divide the nominal Helmholtz free energy density function into an elastic part $\tilde{W}^{\mathrm{elastic}}(\mathbf{F})$ as a function of the deformation gradient $\mathbf{F}$, and a magnetic part $\tilde{W}^{\mathrm{magnetic}}(\mathbf{F},\tilde{\mathbf{B}})$ as a function of the deformation gradient $\mathbf{F}$ and the nominal magnetic flux density $\tilde{\mathbf{B}}$ with the state parameter $\tilde{\mathbf{B}}^{\mathrm{r}}$. This separation ensures that we can link the elastic part to any of the commonly used constitutive models for soft materials such as neo-Hookean, Gent (1996), Arruda and Boyce (1993), and Ogden (1972) among others.

For the magnetic part of the nominal Helmholtz free energy density function, we propose a model of what we define as an *ideal hard-magnetic soft material*. Based on physical observations (Bertotti, 1998), we stipulate that the magnetic flux density $\mathbf{B}$ of the hard-magnetic soft material in the reference configuration is linearly related to the applied magnetic field $\mathbf{H}$ when the field strength is far below the coercivity of the embedded hard-magnetic material (Fig. 3). As the field strength approaches the coercivity $\mathbf{H}^{\mathrm{c}}$, the $\mathbf{B}$-$\mathbf{H}$ relation becomes nonlinear; and the residual magnetic flux density $\mathbf{B}^{\mathrm{r}}$ can be reversed when the applied field strength keeps increasing and exceeds the coercivity $\mathbf{H}^{\mathrm{c}}$ (Fig. 3a). Since the field strength required for

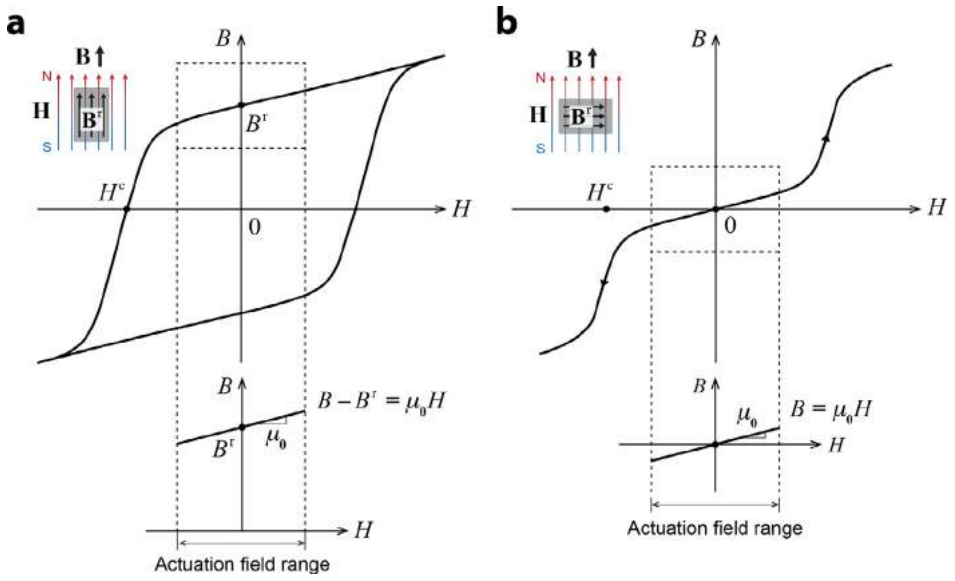

Fig. 3. Linear relation between the applied actuation field and the magnetic flux density of ideal hard-magnetic materials when the residual magnetic flux is (a) parallel and (b) perpendicular to the applied magnetic field. Once magnetically saturated, the linear region of the *B-H* curve for ideal hard-magnetic materials has a slope of vacuum permeability μ_0.

actuating hard-magnetic soft materials is far lower than the coercivity at which the remnant magnetization reversal takes place, it is reasonable to assume that **H** is linearly related to **B** within the working range of magnetic fields for actuation. It should be noted that this linear relation between **B** and **H** must hold regardless of whether or not the sample's residual magnetic flux density $\mathbf{B}^r$ is aligned with the external magnetic field **H**. For example, even when the sample's $\mathbf{B}^r$ is perpendicular to **H**, the measured magnetic flux density **B** along the direction of **H** should linearly depend on **H** (Fig. 3b). This model implies that, as long as the embedded hard-magnetic materials are magnetically saturated, the residual magnetic flux density $\mathbf{B}^r$ of the ideal hard-magnetic soft material remains constant, independently of the external field **H** within the working range for actuation (Fig. 3).

In addition, since the saturation implies that all magnetizable moments have been aligned with the applied field (for saturating the material) (Bertotti, 1998), it is also reasonable to assume that the permeability of saturated hard-magnetic materials is close to that of vacuum or air. Furthermore, considering that the permeability of polymeric matrices such as silicone rubbers is also approximately the same as that of vacuum or air, we further assume that, for ideal hard-magnetic soft materials, the slope of the linear relation between **B** and **H** within the actuation field range is determined by the vacuum (or air) permeability μ_0 as follows:

$$\mathbf{H} = \frac{1}{\mu_0}(\mathbf{B} - \mathbf{B}^r). \tag{3.6}$$

3.4. Calculation of deformation and stress

The constitutive assumptions made in the preceding section, while quite physical, represent an enormous simplification in the mechanics characterization of the hard-magnetic soft material. In particular, the observation that we may, justifiably, assume the vacuum permeability for the ideal hard-magnetic soft material simplifies the solution of what would otherwise be a complex nonlinear mechanics problem.

Based on the model of ideal hard-magnetic soft materials, as illustrated in Fig. 4, we can derive the magnetic part of the Helmholtz free energy and therefore the stress developed in the material under the influence of external magnetic fields as what follows. First, consider a uniform[3] magnetic field **H** generated by a pair of electromagnetic coils in air (Fig. 4a). The applied magnetic flux density $\mathbf{B}^{\text{applied}}$ is then equal to $\mu_0\mathbf{H}$. Then, we introduce a soft material such as an elastomer with zero residual magnetic flux density ($\mathbf{B}^r = \mathbf{0}$) and the permeability of μ_0 to occupy a certain region of the space (Fig. 4b). Since the magnetic permeability is assumed to be the same as that of the ambient media (free space), the presence of this soft material will not perturb the applied magnetic flux density $\mathbf{B}^{\text{applied}}$ or the magnetic Helmholtz free energy. In other words, the soft material will not deform under the applied magnetic field.

[3] The uniform magnetic field is considered for simplicity; however, the theory presented in this paper can also be applied to a non-uniform magnetic field.

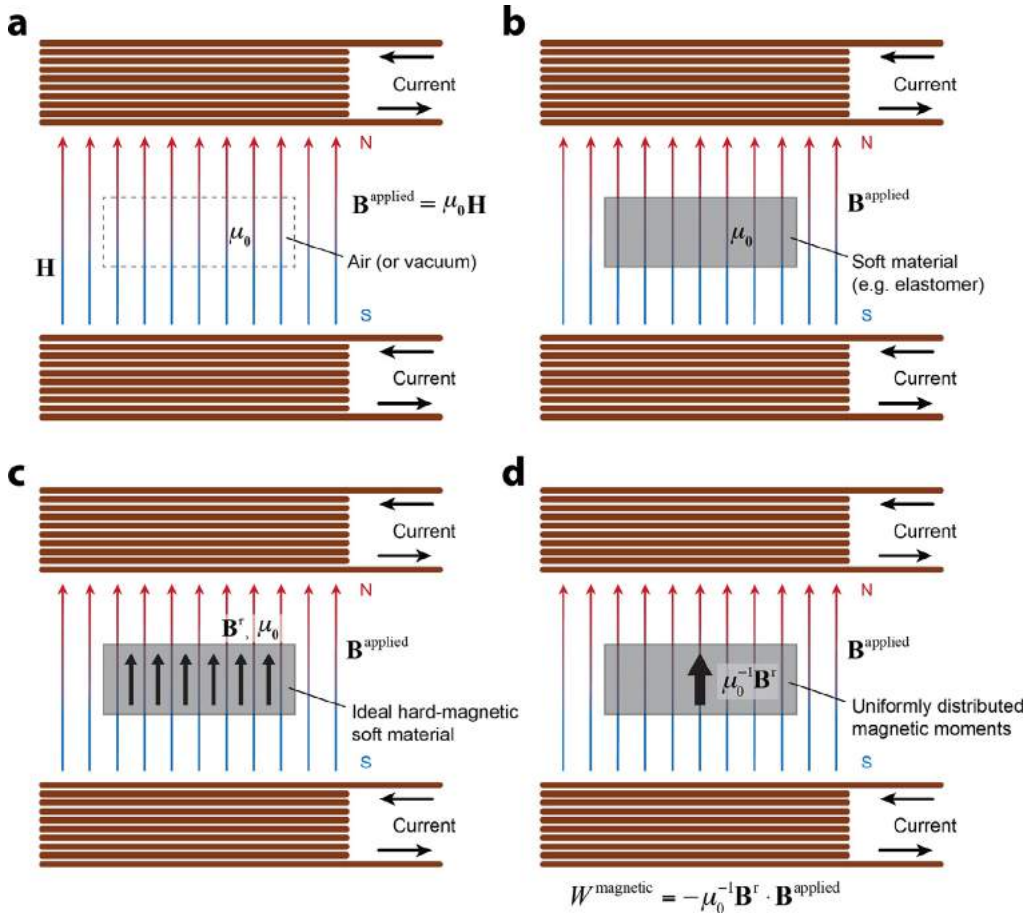

Fig. 4. (a) A magnetic field generated by a pair of electromagnetic coils in air (or vacuum). (b) A non-magnetic soft material with $\mathbf{B}^{\text{r}}=\mathbf{0}$ and permeability of μ_0 occupies a certain region of the space in which a magnetic field is applied. (c) An ideal hard-magnetic soft material with $\mathbf{B}^{\text{r}}$ occupies a certain region of the space with the applied magnetic field. (d) Since the permeability of the ideal hard-magnetic soft material is μ_0, the effect of the $\mathbf{B}^{\text{r}}$ in the applied $\mathbf{B}^{\text{applied}}$ is equivalent to a field of magnetic moments with volumetric density $\mu_0^{-1}\mathbf{B}^{\text{r}}$ in the current configuration.

Next, consider an ideal hard-magnetic soft material placed in the ambient media under the uniform magnetic field (Fig. 4c). The material possesses $\mathbf{B}^{\text{r}}$, which is acquired after being exposed to a strong magnetizing field to magnetically saturate the embedded hard-magnetic particles. Since the permeability of the whole material is μ_0, as discussed earlier, it can be thought that the material possesses the remnant magnetization $\mu_0^{-1}\mathbf{B}^{\text{r}}$, or the remnant magnetic moment per unit volume, which is uniformly distributed in the material in the current configuration (Fig. 4d). Then, we can define the magnetic potential energy, or the magnetic part of the Helmholtz free energy, per unit volume in the current configuration as the work required to realign the magnetic moment $\mu_0^{-1}\mathbf{B}^{\text{r}}$ along the applied magnetic field $\mathbf{B}^{\text{applied}}$ (Bertotti, 1998) as follows:

$$W^{\text{magnetic}} = -\frac{1}{\mu_0}\mathbf{B}^{\text{r}} \cdot \mathbf{B}^{\text{applied}}. \tag{3.7}$$

Then, from the relation $\tilde{W}^{\text{magnetic}} = W^{\text{magnetic}} J$ and Eq. (3.3), the magnetic Helmholtz free energy per unit reference volume can be expressed as

$$\tilde{W}^{\text{magnetic}} = -\frac{1}{\mu_0}\mathbf{F}\tilde{\mathbf{B}}^{\text{r}} \cdot \mathbf{B}^{\text{applied}}. \tag{3.8}$$

Once a hard-magnetic material is magnetically saturated, the $\tilde{\mathbf{B}}^{\text{r}}$ of the material is fixed unless a strong demagnetizing field beyond the coercivity $\mathbf{H}^{\mathbf{c}}$ is applied (Fig. 1). Therefore, Eq. (3.8) implies that rigid-body rotation of a hard-magnetic material under the applied field $\mathbf{B}^{\text{applied}}$ can vary the magnetic Helmholtz free energy of the material. In general, rigid-body rotation can change the free energies of polar continua as well.

Overall, the combined total Helmholtz free energy of the ideal hard-magnetic soft material per unit volume in the reference configuration can be expressed as

$$\tilde{W} = \tilde{W}^{\text{elsastic}}(\mathbf{F}) - \frac{1}{\mu_0}\mathbf{F}\tilde{\mathbf{B}}^{\text{r}} \cdot \mathbf{B}^{\text{applied}}. \tag{3.9}$$

Here, we remark that $\tilde{W}$ is a function of $\mathbf{F}$ only, because $\tilde{\mathbf{B}}^{\mathrm{r}}$ and $\mathbf{B}^{\mathrm{applied}}$ are already specified as constant values at each location of interest. By substituting Eq. (3.9) into Eq. (3.4a), we can obtain the first Piola–Kirchoff stress as

$$\mathbf{P} = \frac{\partial \tilde{W}^{\mathrm{elsastic}}(\mathbf{F})}{\partial \mathbf{F}} - \frac{1}{\mu_0}\mathbf{B}^{\mathrm{applied}} \otimes \tilde{\mathbf{B}}^{\mathrm{r}}, \tag{3.10}$$

where the operation $\otimes$ denotes the dyadic product, which takes two vectors to yield a second order tensor. By converting nominal quantities into true quantities, we further obtain the Cauchy stress as

$$\boldsymbol{\sigma} = \frac{1}{J}\frac{\partial \tilde{W}^{\mathrm{elsastic}}(\mathbf{F})}{\partial \mathbf{F}}\mathbf{F}^{\mathrm{T}} - \frac{1}{\mu_0 J}\mathbf{B}^{\mathrm{applied}} \otimes \mathbf{F}\tilde{\mathbf{B}}^{\mathrm{r}} = \frac{1}{J}\frac{\partial \tilde{W}^{\mathrm{elsastic}}(\mathbf{F})}{\partial \mathbf{F}}\mathbf{F}^{\mathrm{T}} - \frac{1}{\mu_0}\mathbf{B}^{\mathrm{applied}} \otimes \mathbf{B}^{\mathrm{r}}. \tag{3.11}$$

Since $\mathbf{B}^{\mathrm{applied}}$ and $\tilde{\mathbf{B}}^{\mathrm{r}}$ are known, the stress tensors $\mathbf{P}$ and $\boldsymbol{\sigma}$ are functions of the deformation gradient $\mathbf{F}$ only. By substituting Eqs. (3.10) and (3.11) and the boundary conditions into the equilibrium equations in Eqs. (2.6) and (2.7), we can calculate the deformation gradient $\mathbf{F}$, which will allow us to quantify how the hard-magnetic soft material deforms under the applied magnetic field.

In addition, we can express the body torque (i.e. the torque per unit volume of the material in the current state) generated by the magnetized domain under the applied magnetic field as

$$\mathbf{m} = \frac{1}{\mu_0}\mathbf{B}^{\mathrm{r}} \times \mathbf{B}^{\mathrm{applied}} \tag{3.12}$$

By substituting Eqs. (3.11) and (3.12) into Eq. (2.9), we find that the concervation of angular momentum is satisfied by the constitutive model of ideal hard-magnetic soft materials.

4. Numerical implementation

As detailed in preceding sections, the proposed constitutive law aims to describe the mechanical response of hard-magnetic soft materials under an applied magnetic field. To account for the magnetically induced asymmetric stress contribution, we implement the developed constitutive law in the form of a user-defined element subroutine (UEL) in Abaqus/Standard (2016). We note that due to the constitutive choice of an ideal hard-magnetic soft material, and $\mathbf{B}^{\mathrm{applied}}$ directly prescribed, the governing Eq. (2.10a) and (2.10b) and associated boundary conditions (2.14a) and (2.14b) are satisfied.

4.1. Boundary-value problem

To begin, we summarize the governing partial differential equations and the weak form for the deformed body B_t (Henann et al., 2013; Wang et al., 2016; Chester et al., 2015). With body forces denoted by $\mathbf{f}$, the equilibrium equation is,

$$\mathrm{div}\,\boldsymbol{\sigma} + \mathbf{f} = \mathbf{0} \quad \text{in} \quad \mathrm{B}_t, \tag{4.1}$$

In the absence of applied tractions, the mechanical boundary conditions on the current surface $\partial \mathrm{B}_t$ are given by

$$\mathbf{u} = \breve{\mathbf{u}} \quad \text{on} \quad \mathrm{S}_{\mathbf{u}}, \quad \text{and} \quad \boldsymbol{\sigma}\mathbf{n} = \mathbf{0} \quad \text{on} \quad \mathrm{S}_t, \tag{4.2}$$

where $\breve{\mathbf{u}}$ is the prescribed displacements, and $\mathrm{S}_{\mathbf{u}}$ and S_t are complementary subsurfaces of $\partial \mathrm{B}_t$. With $\mathbf{w}$ denoting the weighting field, the corresponding weak form of the boundary-value problem from Eqs. (4.1) to (4.2) is expressed as

$$\int_{\mathrm{B}_t} \left(\boldsymbol{\sigma} : \frac{\partial \mathbf{w}}{\partial \mathbf{x}} \right) dv = \int_{\mathrm{B}_t} (\mathbf{w} \cdot \mathbf{f}) dv, \tag{4.3}$$

where the operator : denotes the double contraction of two tensors as previously. Next, the deformed body is approximated using finite-elements, $\mathrm{B}_t = \cup \mathrm{B}_t{}^e$, and the displacement vector is the nodal solution variable. The displacement vector is interpolated inside each element by

$$\mathbf{u} = \sum \mathbf{u}^A N^A, \tag{4.4}$$

where the index $A = 1, 2, \ldots$ denotes the nodes of the element, $\mathbf{u}^A$ denote the nodal displacements, and N^A are the shape functions. By employing a standard Galerkin approach, the weighting field is interpolated by the same shape functions as

$$\mathbf{w} = \sum \mathbf{w}^A N^A. \tag{4.5}$$

Then the element-level residual for the displacement is

$$(\mathbf{R_u})^A = \int_{B_t{}^e} \left(\boldsymbol{\sigma}\frac{\partial N^A}{\partial \mathbf{x}}\right) dv - \int_{B_t{}^e} \left(N^A \mathbf{f}\right) dv. \tag{4.6}$$

Eq. (4.6) is solved iteratively using a Newton–Raphson procedure, using the appropriate material tangents, which is given by

$$(\mathbf{K_{uu}})^{AB} = -\frac{\partial (\mathbf{R_u})^A}{\partial \mathbf{u}^B}. \tag{4.7}$$

As repeatedly discussed earlier, the Cauchy stress in Eq. (4.1) can be asymmetric due to the presence of body torques. This point requires special attention since most commercial finite-element packages assume the Cauchy stress to be symmetric, which is true from conservation of the angular momentum only if there exist no body torques (i.e. in non-polar continua).

4.2. Complete form of Cauchy stress and material tangent for finite-element implementation

As derived in Section 3, the nominal Helmholtz free energy density function of the ideal hard-magnetic soft material is given by Eq. (3.9). Adopting the neo-Hookean constitutive model[4] for the purely mechanical (elastic) response of the proposed material, the complete nominal Helmholtz free energy density function can be expressed as

$$\tilde{W} = \frac{G}{2}\left(J^{-2/3} I_1 - 3\right) + \frac{K}{2}(J-1)^2 - \frac{1}{\mu_0}\mathbf{F}\tilde{\mathbf{B}}^{\mathrm{r}} \cdot \mathbf{B}^{\mathrm{applied}}, \tag{4.8}$$

where G is the shear modulus, K is the bulk modulus, and $I_1 = \mathrm{tr}(\mathbf{F}^{\mathrm{T}}\mathbf{F})$. From Eq. (3.10), the first Piola–Kirchhoff stress can be calculated as

$$\mathbf{P} = GJ^{-2/3}\left(\mathbf{F} - \frac{I_1}{3}\mathbf{F}^{-\mathrm{T}}\right) + KJ(J-1)\mathbf{F}^{-\mathrm{T}} - \frac{1}{\mu_0}\mathbf{B}^{\mathrm{applied}} \otimes \tilde{\mathbf{B}}^{\mathrm{r}}, \tag{4.9}$$

with its elastic and magnetic contributions expressed as

$$\mathbf{P}^{\mathrm{elastic}} = GJ^{-2/3}\left(\mathbf{F} - \frac{I_1}{3}\mathbf{F}^{-\mathrm{T}}\right) + KJ(J-1)\mathbf{F}^{-\mathrm{T}}, \tag{4.10a}$$

$$\mathbf{P}^{\mathrm{magnetic}} = -\frac{1}{\mu_0}\mathbf{B}^{\mathrm{applied}} \otimes \tilde{\mathbf{B}}^{\mathrm{r}}. \tag{4.10b}$$

Then, the total Cauchy stress can be calculated from the first Piola–Kirchhoff stress as

$$\boldsymbol{\sigma} = \frac{1}{J}\mathbf{P}\mathbf{F}^{\mathrm{T}} = GJ^{-5/3}\left(\mathbf{F}\mathbf{F}^{\mathrm{T}} - \frac{I_1}{3}\mathbf{I}\right) + K(J-1)\mathbf{I} - \frac{1}{\mu_0 J}\mathbf{B}^{\mathrm{applied}} \otimes \mathbf{F}\tilde{\mathbf{B}}^{\mathrm{r}}, \tag{4.11}$$

with its elastic and magnetic contributions expressed as

$$\boldsymbol{\sigma}^{\mathrm{elastic}} = GJ^{-5/3}\left(\mathbf{F}\mathbf{F}^{\mathrm{T}} - \frac{I_1}{3}\mathbf{I}\right) + K(J-1)\mathbf{I}, \tag{4.12a}$$

$$\boldsymbol{\sigma}^{\mathrm{magnetic}} = -\frac{1}{\mu_0 J}\mathbf{B}^{\mathrm{applied}} \otimes \mathbf{F}\tilde{\mathbf{B}}^{\mathrm{r}} = -\frac{1}{\mu_0}\mathbf{B}^{\mathrm{applied}} \otimes \mathbf{B}^{\mathrm{r}}. \tag{4.12b}$$

Evidently, if $\mathbf{B}^{\mathrm{applied}}$ is aligned with $\mathbf{B}^{\mathrm{r}}$ in the current state, the cross-product vanishes and the stress becomes symmetric. In the more general case, however, both the total Cauchy stress $\boldsymbol{\sigma}$ and the magnetic Cauchy stress $\boldsymbol{\sigma}^{\mathrm{magnetic}}$ are asymmetric. Next, we calculate the material tangent based on the first Piola–Kirchhoff stress. The elastic and magnetic contributions of the material tangent are defined and calculated through

$$\begin{aligned}\frac{\partial P_{ij}^{\mathrm{elastic}}}{\partial F_{kl}} &= GJ^{-2/3}\left[-\frac{2}{3}F_{ij}F_{lk}^{-1} + \frac{2}{9}I_1 F_{ji}^{-1}F_{lk}^{-1} + \delta_{ik}\delta_{jl} - \frac{2}{3}F_{kl}F_{ji}^{-1} + \frac{I_1}{3}F_{li}^{-1}F_{jk}^{-1}\right] \\ &\quad + KJ\left[(2J-1)F_{ji}^{-1}F_{lk}^{-1} - (J-1)F_{li}^{-1}F_{jk}^{-1}\right],\end{aligned} \tag{4.13a}$$

$$\frac{\partial P_{ij}^{\mathrm{magnetic}}}{\partial F_{kl}} = \frac{\partial\left(-\mu_0^{-1}B_i^{\mathrm{applied}}\tilde{B}_j^{r}\right)}{\partial F_{kl}} = 0. \tag{4.13b}$$

[4] This choice is not essential to the central theme of the present work. Any suitable mechanical constitutive law may be adopted depending on the desired fidelity and ramifications of the attendant complexity.

From Eq. (4.13b) we can see that the magnetic potential energy does not contribute to the material tangent based on the first Piola–Kirchhoff stress. Finally, the spatial tangent C_{ijkl} is further calculated through

$$C_{ijkl} = J^{-1} F_{jm} F_{ln} \frac{\partial P^{\text{elastic}}_{im}}{\partial F_{kn}}. \tag{4.14}$$

Eqs. (4.11)–(4.14) were programmed in a user-element subroutine (UEL), following the finite-element procedures described in Section 4.1. To address the volumetric-locking issue caused by the material's near incompressibility, the F-bar formulation (de Souza Neto et al., 1996) was used for fully integrated elements. During the finite-element simulation, the UEL is called for each iteration in a given increment to provide the residual and consistent tangent. In addition, the material parameters, including shear modulus G, bulk modulus K, residual magnetic flux density $\tilde{\mathbf{B}}^{\text{r}}$, and applied magnetic flux density vector $\mathbf{B}^{\text{applied}}$, are prescribed in the input file. These parameters, together with the current values of the nodal displacements, are used to calculate the residuals and consistent tangents. Here, to implement the three-dimensional actuation of the hard-magnetic soft material, we developed an eight-noded brick user-element. Unlike that conventional 8-noded brick elements consider only six independent components of a Cauchy stress tensor under the assumption of symmetry, our user-element developed for hard-magnetic materials deals with all nine components of the Cauchy stress tensor due to the possible asymmetry. For objects with multiple hard-magnetic domains, the geometry is divided into sections that are assigned with parameters independently with predefined material properties[5].

5. Validation of the model for hard-magnetic soft materials

In this section, we first verify that our model is correctly implemented and gives simulation results consistent with analytical predictions. For this verification, we compare the simulation and analytical results for the following two simple cases with magnetically induced deformation: (i) homogeneous uniaxial deformation of a cube (Section 5.2) and (ii) small-deflection bending of a beam (Section 5.3), both of which can be analytically solved. We also validate the physics underpinning the developed model by comparing our model-based simulation and experimental results for both small and large bending cases. For small bending, the experimentally measured beam deflections are compared with both the analytical solutions and the simulation results. To validate our model-based simulation for large bending, which has no tractable analytical solutions, we compare the experimental and simulation results in terms of the maximal deflection and the actuation angle. The input parameters used in the simulation were obtained from measurement.

5.1. Material preparation and characterization

Hard-magnetic soft materials for the experimental validation were prepared by mixing NdFeB microparticles with PDMS (Sylgard 184) at prescribed volume fractions. The mixture was poured into a mold to obtain desired geometry and then cured at 120 °C for 1hr. After curing, the material was uniformly magnetized by applying an impulse magnetic field, after which the resulting residual magnetic flux density $\tilde{\mathbf{B}}^{\text{r}}$ was measured. Then, the shear modulus G of the material was evaluated by curve-fitting the tensile testing data with the isotropic neo-Hookean model. Exact numbers for the material properties are provided from Sections 5.3 to 5.5 in which we describe each set of experiments more in detail. The measured material properties such as the shear modulus G and the residual magnetic flux density $\tilde{\mathbf{B}}^{\text{r}}$ were reflected in the input files generated in Abaqus/Standard and passed on to the UEL while running the simulation. The bulk modulus K was chosen to satisfy $K = 1000\,G$ to approximate near incompressibility. The uniform magnetic field $\mathbf{B}^{\text{applied}}$ applied for actuation was also defined in the input file.

5.2. Homogeneous uniaxial actuation of a cube

First, we consider a cubic body whose edges are aligned with 1,2,3-directions (Fig. 5a). We assume that both the residual magnetic flux density $\tilde{\mathbf{B}}^{\text{r}}$ and the applied magnetic flux density $\mathbf{B}^{\text{applied}}$ are parallel to the 2-direction in the reference configuration. As shown in Fig. 5b and c, the resultant homogeneous uniaxial deformation occurs along the 2-direction, with the principal stretch $\lambda_2 = \lambda$. The other two principal stretches are also aligned with the edges of the cube in 1- and 3-directions, giving λ_1 and λ_3, respectively. For the analytical result, we assume that the material is nearly incompressible ($\lambda_1\lambda_2\lambda_3 = 1, J = 1$), and therefore the deformation gradient tensor can be expressed as

$$[\mathbf{F}] = \begin{bmatrix} \lambda^{-1/2} & 0 & 0 \\ 0 & \lambda & 0 \\ 0 & 0 & \lambda^{-1/2} \end{bmatrix}. \tag{5.1}$$

Under the same condition of incompressibility, the analytic Cauchy stress can be written as

$$\boldsymbol{\sigma} = G\mathbf{F}\mathbf{F}^{\text{T}} - p\mathbf{I} - \frac{1}{\mu_0}\mathbf{B}^{\text{applied}} \otimes \mathbf{F}\tilde{\mathbf{B}}^{\text{r}}, \tag{5.2}$$

[5] Our Abaqus user-element subroutine and input file demonstrating magnetic-induced simple beam bending can be made available upon request.

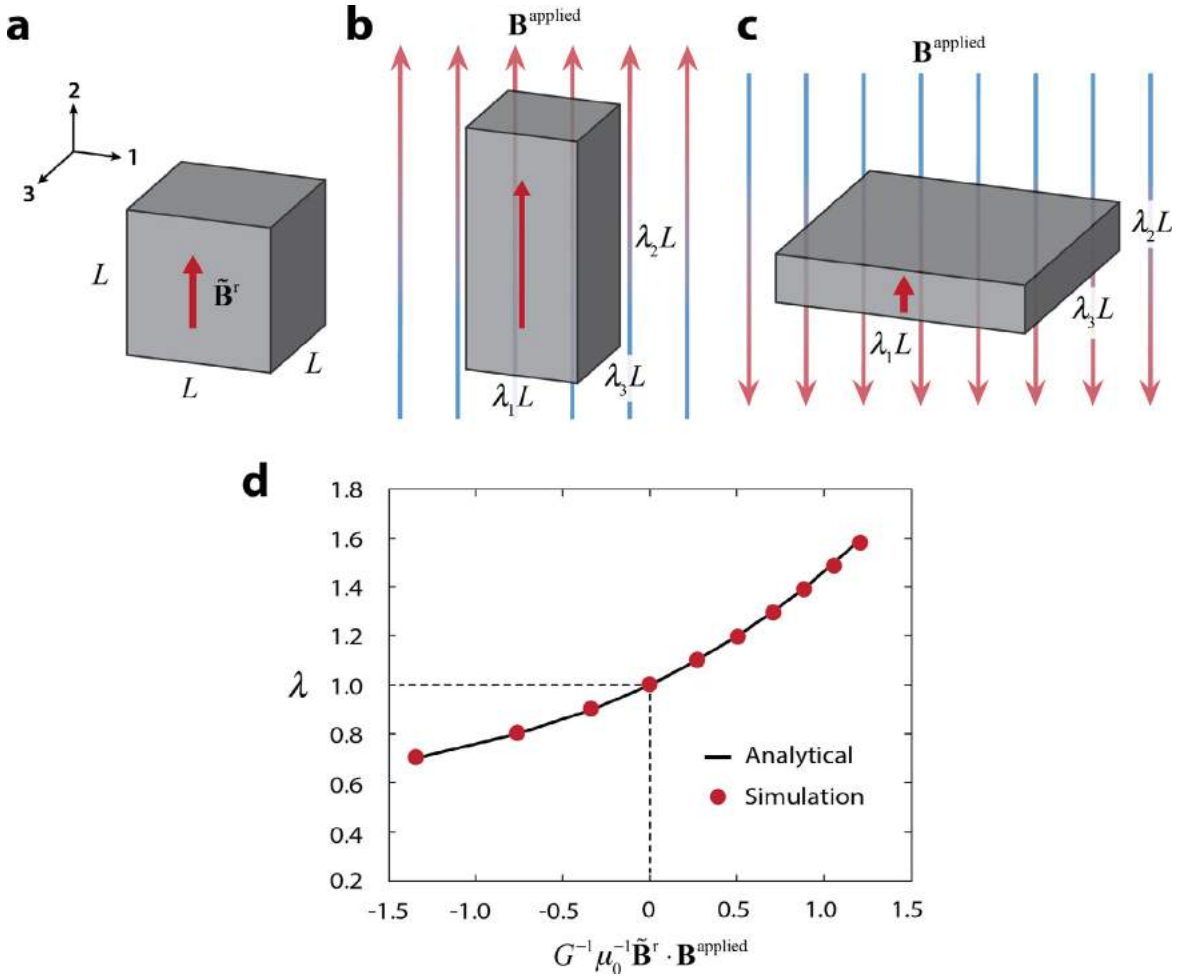

Fig. 5. Verification of the UEL subroutine for the case of uniaxial homogeneous magnetic actuation. (a) An undeformed cube with edge length L and the residual magnetic flux density $\tilde{\mathbf{B}}^{\mathrm{r}}$ along the 2-direction. (b) Homogeneous elongation of the cube under a uniform magnetic field $\mathbf{B}^{\mathrm{applied}}$ applied along the positive 2-direction. (c) Homogeneous shortening of the cube under a uniform magnetic field $\mathbf{B}^{\mathrm{applied}}$ applied along the negative 2-direction. (d) Relationship between the homogeneous uniaxial stretch and the normalized magnetic flux density (adapted and modified from (Kim et al., 2018)).

where p is the hydrostatic pressure which can be determined from boundary conditions. From Eq. (5.2), three components of the Cauchy stress along the principal directions can be expressed as

$$\sigma_{22} = G\lambda^2 - p - \frac{\lambda}{\mu_0}\tilde{\mathbf{B}}^{\mathrm{r}} \cdot \mathbf{B}^{\mathrm{applied}}, \tag{5.3a}$$

$$\sigma_{11} = \sigma_{33} = \frac{G}{\lambda} - p, \tag{5.3b}$$

where the traction-free boundary condition yields $\sigma_{11} = \sigma_{22} = \sigma_{33} = 0$. By subtracting Eq. (5.3b) from Eq. (5.3a) and rearranging the expression, we obtain the following dimensionless relation which determines the magnetically induced elongation or shortening depending on the strength and direction of the applied magnetic field as well as the shear modulus G:

$$\lambda - \frac{1}{\lambda^2} = \frac{1}{\mu_0 G}\tilde{\mathbf{B}}^{\mathrm{r}} \cdot \mathbf{B}^{\mathrm{applied}}. \tag{5.4}$$

This homogenous deformation under the uniaxial actuation of a cube was simulated with a single eight-noded user element we developed. Fig. 5d depicts the relationship between the stretch and the dimensionless quantity $G^{-1}\mu_0^{-1}\tilde{\mathbf{B}}^{\mathrm{r}} \cdot \mathbf{B}^{\mathrm{applied}}$, which we refer to as the normalized magnetic flux density applied for actuation. The simulation results are in good agreement with the closed-form analytical solution given by Eq. (5.4). The case when $G^{-1}\mu_0^{-1}\tilde{\mathbf{B}}^{\mathrm{r}} \cdot \mathbf{B}^{\mathrm{applied}} = 0$ corresponds to the undeformed reference state in the absence of external magnetic fields. When the actuation field is applied along the material's remanence, i.e. $G^{-1}\mu_0^{-1}\tilde{\mathbf{B}}^{\mathrm{r}} \cdot \mathbf{B}^{\mathrm{applied}} > 0$, the magnetic stress causes elongation ($\lambda > 1$) of the cube (Fig. 5b). When

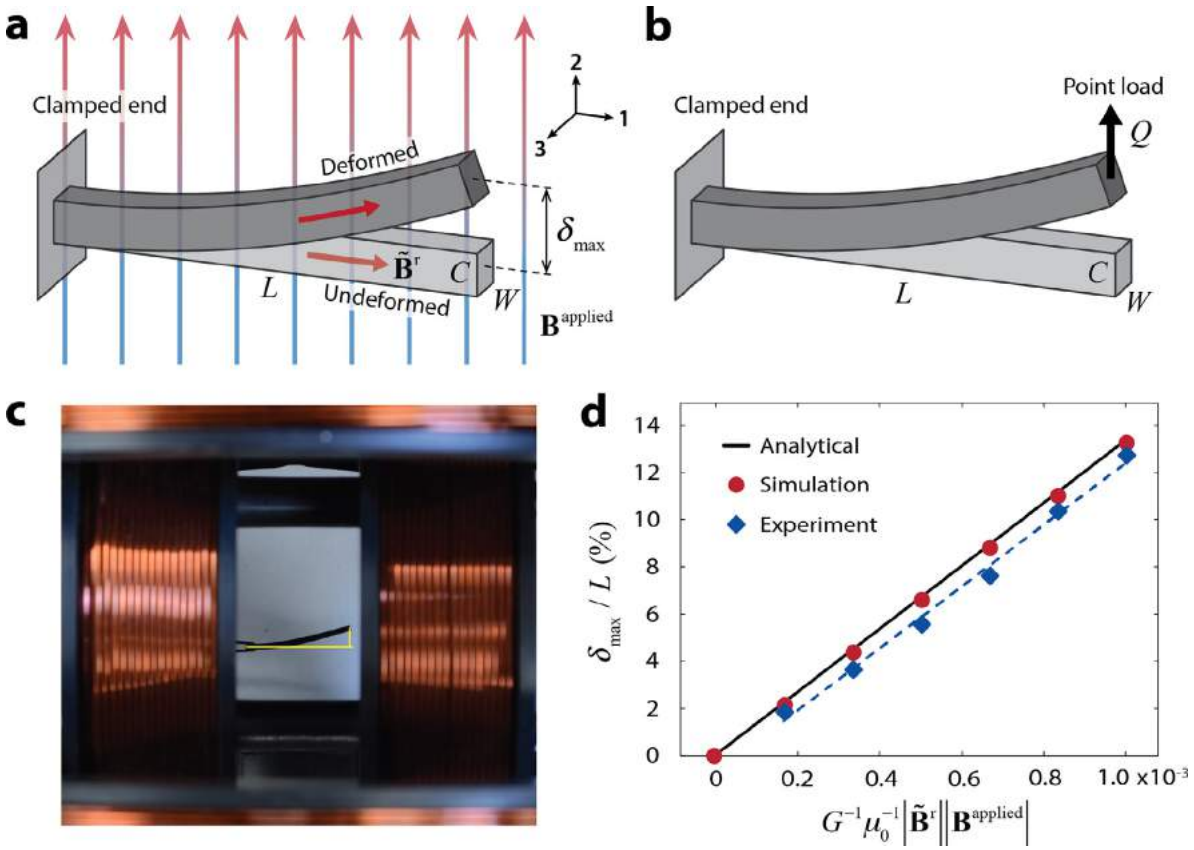

Fig. 6. Validation of the UEL subroutine for the magnetically actuated beam bending with small deflection. (a) Schematic of the actuation of a beam whose residual magnetic flux density $\tilde{\mathbf{B}}^{\mathrm{r}}$ is aligned with 1-direction. The beam length, width, and thickness are prescribed as L=17.5 mm, W=5 mm, and C=1.75 mm, respectively. During the actuation, one end of the beam is clamped while the remainder is free to bend under a uniform magnetic field applied in the 2-direction, which is perpendicular to the beam length. (b) Equivalent beam bending with small deflection under a point load at the free-end. (c) Experimental setup for beam bending test. The applied magnetic field $\mathbf{B}^{\mathrm{applied}}$ ranged from 0 to 6 mT with 1 mT intervals, which corresponds to a range from 0 to 0.001 in terms of the normalized magnetic flux density $G^{-1}\mu_0^{-1}|\tilde{\mathbf{B}}^{\mathrm{r}}||\mathbf{B}^{\mathrm{applied}}|$. (d) Analytical, simulation, and experiment results which reveal the relationship between the normalized the free-end deflection $\delta_{\max}/L$ and the normalized magnetic flux density $G^{-1}\mu_0^{-1}|\tilde{\mathbf{B}}^{\mathrm{r}}||\mathbf{B}^{\mathrm{applied}}|$ for beams with shear modulus G=1229 kPa and residual magnetic flux density $|\tilde{\mathbf{B}}^{\mathrm{r}}| = 0.258$ T ($\mu_0^{-1}|\tilde{\mathbf{B}}^{\mathrm{r}}| = 205$ kA/m). The dotted line denotes the linear fit of the experimental data points. (For interpretation of the references to color in this figure, the reader is referred to the web version of this article.)

the actuation field is applied in the opposite direction of the remanence, i.e. $G^{-1}\mu_0^{-1}\tilde{\mathbf{B}}^{\mathrm{r}} \cdot \mathbf{B}^{\mathrm{applied}} < 0$, a compressive stress develops, causing the shrinkage ($\lambda < 1$) of the cube along the applied field direction (Fig. 5c).

5.3. Small-deflection beam bending

To further validate our finite-element model for the case of bending induced by magnetic torques, we now set the external magnetic field $\mathbf{B}^{\mathrm{applied}}$ to be applied perpendicularly to the residual magnetic flux density $\tilde{\mathbf{B}}^{\mathrm{r}}$ of a beam made of the hard-magnetic soft material. We begin by considering a small-deflection bending case, for which we can find analytical solutions, with a rectangular beam of length $L = 17.5$ mm, width $W = 5$ mm, and thickness $C = 1.75$ mm (L / $C = 10$) with uniform $\tilde{\mathbf{B}}^{\mathrm{r}}$ along the length direction (the 1-direction) as depicted in Fig. 6a. One end of the beam is clamped while the remainder is free to move under the action of the uniform magnetic field $\mathbf{B}^{\mathrm{applied}}$ applied perpendicularly to $\tilde{\mathbf{B}}^{\mathrm{r}}$ (i.e. in the 2-direction). We define small bending as the maximal deflection of the free end, denoted by $\delta_{\max}$, being smaller than 10% of the beam length L. Magnetic torques generated by the embedded magnetic dipoles under the applied field induce stresses that collectively lead to the deflection of the beam. For small deflection of an incompressible solid, the only non-zero term of the magnetic Cauchy stress is $\sigma_{21}^{\mathrm{magnetic}} = -\mu_0^{-1}|\tilde{\mathbf{B}}^{\mathrm{r}}||\mathbf{B}^{\mathrm{applied}}|$ as calculated from Eq. (4.11).

To obtain the maximal deflection, we first evaluate the magnetically induced moment dM for an incremental volume dV of the beam as $dM = \mu_0^{-1}|\tilde{\mathbf{B}}^{\mathrm{r}}||\mathbf{B}^{\mathrm{applied}}|dV = \mu_0^{-1}|\tilde{\mathbf{B}}^{\mathrm{r}}||\mathbf{B}^{\mathrm{applied}}|WCdx$, with dx denoting an incremental length along the beam length direction. Therefore, the magnetic torque at position x on the beam can be expressed as

$$M(x) = \mu_0^{-1}|\tilde{\mathbf{B}}^{\mathrm{r}}||\mathbf{B}^{\mathrm{applied}}|WC(L-x). \tag{5.5}$$

This effective moment distribution along the beam is equivalent to that generated by a point force Q applied at the free end of the beam along the direction of the applied magnetic field (Fig. 6b), where Q can be expressed as

$$Q \equiv |dM/dx| = \mu_0^{-1}|\tilde{\mathbf{B}}^{\mathrm{r}}||\mathbf{B}^{\mathrm{applied}}|WC. \tag{5.6}$$

With the area moment of inertia I defined as $I = WC^3/12$, the bending stiffness of the beam can be calculated as $K_b = 3EI/L^3 = 3GWC^3/(4L^3)$. Then the maximal deflection of the beam $\delta_{\max}$ by the action of the point load Q at the free end can be calculated through $\delta_{\max} = Q/K_b$ in a dimensionless form as

$$\frac{\delta_{\max}}{L} = \frac{4|\tilde{\mathbf{B}}^{\mathrm{r}}||\mathbf{B}^{\mathrm{applied}}|L^2}{3\mu_0 GC^2}. \tag{5.7}$$

This analytical prediction shows that the normalized beam deflection $\delta_{\max}/L$ is linearly related with the dimensionless quantity, or the normalized magnetic flux density, $G^{-1}\mu_0^{-1}|\tilde{\mathbf{B}}^{\mathrm{r}}||\mathbf{B}^{\mathrm{applied}}|$.

To experimentally validate the analytical and numerical predictions for small deflection of a beam, we prepared a beam with exact dimensions as mentioned previously (length $L = 17.5$ mm, width $W = 5$ mm, and thickness $C = 1.75$ mm), following the material preparation procedure in Section 5.1. For the small bending case, 40% of magnetic particles in terms of volume fraction was used to increase the beam stiffness. The average shear modulus of the specimens was $G = 1229$ kPa, and the remanence magnitude was measured to be $|\tilde{\mathbf{B}}^{\mathrm{r}}| = 0.258$ T ($\mu_0^{-1}|\tilde{\mathbf{B}}^{\mathrm{r}}| = 205$ kA/m). Before actuation, one end of the beam was clamped by a tweezer to impose the fixed boundary condition in Fig. 6a. The beam was then placed in a uniform magnetic field generated by two-axes Helmholtz coils as shown in Fig. 6c. Since the external magnetic field was applied in the horizontal plane perpendicular to the beam length direction, the gravitational effect played no role in the beam deformation. To satisfy the assumption of small deflection ($\delta_{\max}/L < 10\%$), the applied magnetic flux density was controlled within the range from 0 to 6 mT with 1 mT intervals, which corresponds to a range from 0 to 0.001 in terms of the normalized magnetic flux density $G^{-1}\mu_0^{-1}|\tilde{\mathbf{B}}^{\mathrm{r}}||\mathbf{B}^{\mathrm{applied}}|$.

Fig. 6d shows the normalized deflection $\delta_{\max}/L$ of the beam against the applied magnetic flux density $\mathbf{B}^{\mathrm{applied}}$ to compare the theoretical prediction with the simulation and experimental results. The simulation results (red circles) show good agreement with the analytical solution (solid line) in Eq. (5.7). As predicted by Eq. (5.7), for the small bending case, the experimental results (blue squares) show a linear relation between the normalized deflection and the applied field strength. However, the normalized deflections are overall smaller than the analytical and simulation results, which can be attributed to the imperfect fixed boundary condition at the clamped tip. The use of a tweezer to clamp the end tip, unlike the idealized fixed end, would have slightly reduced the effective beam length, which might lead to the smaller deflections due to the square dependence of L in Eq. (5.7). In addition to this, such small deflections are more susceptible to measurement errors than experimental data for large-deflection bending. For these reasons, we conclude that the linear relation verified from the experimental results is sufficient for validating the analytical model and numerical implementation for small-deflection bending.

5.4. Large-deflection bending up to 90°

While small bending with homogeneous deformation is amenable to comparing our model-based simulation results with both theoretical and experimental data for validation, due mainly to the existence of tractable analytical solutions, large bending is of greater importance in practical applications. We therefore apply our developed model and computational framework to investigate the large deformation as well. Similar to the small bending case described in the preceding section, the beam of length L, width W, and thickness C is considered, whose $\tilde{\mathbf{B}}^{\mathrm{r}}$ is aligned with the 1-direction (Fig. 7a). One end of the beam is clamped, and the remainder is free to move under the action of a uniform magnetic field applied in 2-direction, which is perpendicular to the beam length direction.

The normalized deflection at the end tip, $\delta_{\max}/L$, was measured for beams with four different dimensions (Table 1) and aspect ratios ($L/C = 10,\ 17.5,\ 20.5,\ 41$) while varying the applied magnetic field from 0 to 50 mT, which corresponds to a range from 0 to 0.019 in terms of the normalized magnetic flux density $G^{-1}\mu_0^{-1}|\tilde{\mathbf{B}}^{\mathrm{r}}|\mathbf{B}^{\mathrm{applied}}|$ (Fig. 7b). We also measured the actuation angle θ (Fig. 7c) while varying the applied magnetic field to evaluate the point at which the beam with each aspect ratio reaches the maximum level of actuation ($\theta = 90°$). The actuation angle was defined as the angular deviation of the tangent at the tip from the reference length direction as illustrated in Fig. 7a. The average shear modulus and remanence were measured as $G = 303$ kPa and $|\tilde{\mathbf{B}}^{\mathrm{r}}| = 0.143$ T($\mu_0^{-1}|\tilde{\mathbf{B}}^{\mathrm{r}}| = 114$ kA/m), respectively, which were used in our model-based simulation as input parameters.

Table 1
Beam dimensions for 90° actuation presented in Section 5.4 and Fig. 7.

Aspect ratio L / C	L (mm)	C (mm)	W (mm)
10	11	1.1	5
17.5	19.2	1.1	5
20.5	17.2	0.84	5
41	17.2	0.42	5

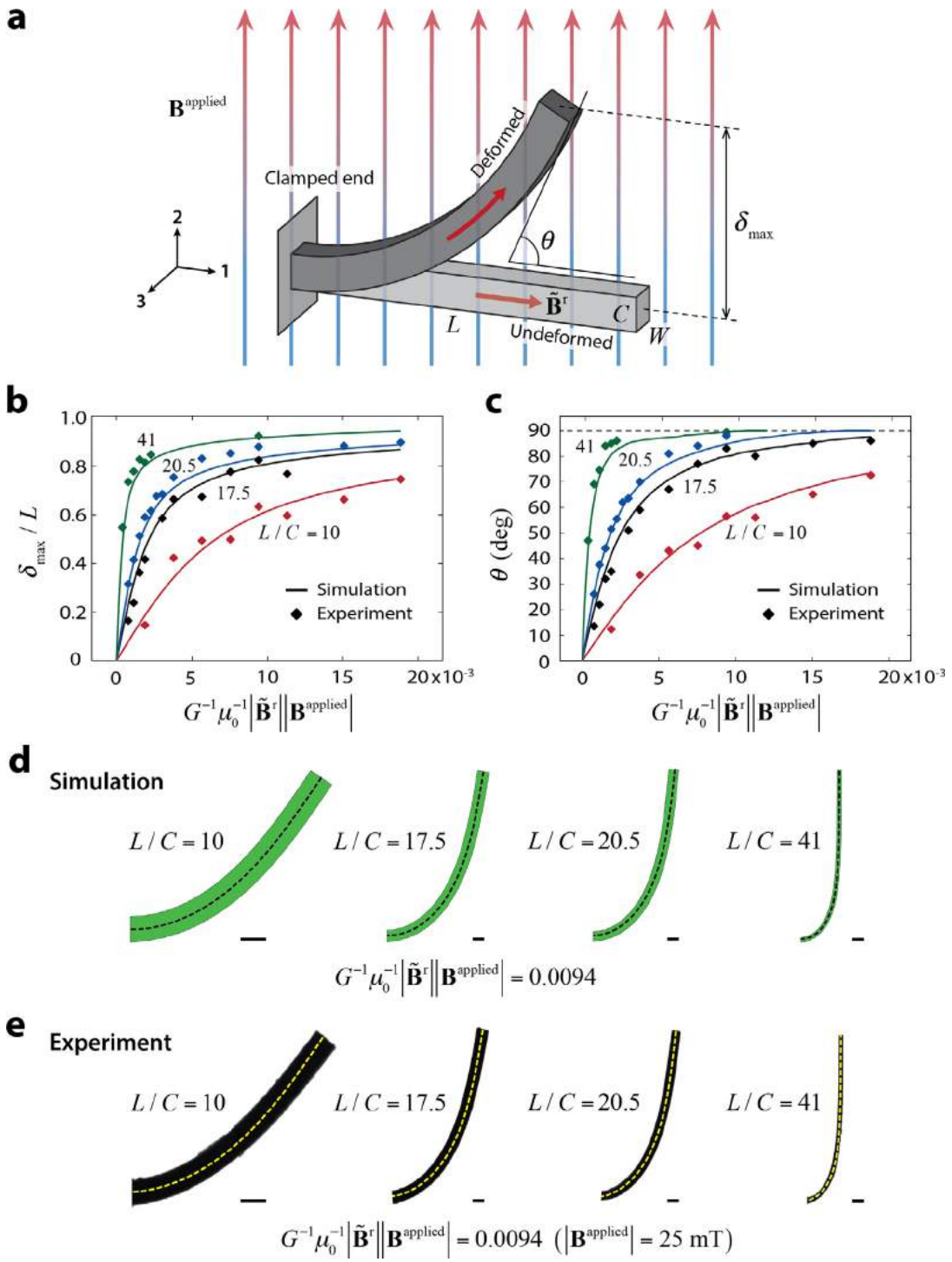

Fig. 7. Validation of the UEL subroutine for the magnetically actuated beam bending with large deflection. (a) Schematic of the actuation of a beam whose initial residual magnetic flux density $\tilde{\mathbf{B}}^{\mathrm{r}}$ is aligned with the 1-direction. During the actuation, one end of the beam is clamped, while the remainder is free to bend under a uniform magnetic field applied in the 2-direction perpendicularly to the beam length. The actuation angle is defined as the angular deviation of the tangent at the tip from the reference length direction. (b) Simulation and experimental results on the relationship between the normalized free-end deflection $\delta_{\max}/L$ and the normalized magnetic flux density $G^{-1}\mu_0^{-1}|\tilde{\mathbf{B}}^{\mathrm{r}}||\mathbf{B}^{\mathrm{applied}}|$, for rectangular beams with the same shear modulus G=303 kPa and residual magnetic flux density $|\tilde{\mathbf{B}}^{\mathrm{r}}| = 0.143\,\mathrm{T}(\mu_0^{-1}|\tilde{\mathbf{B}}^{\mathrm{r}}| = 114\,\mathrm{kA/m})$ but different aspect ratios $L\,/\,C$ = 10, 17.5, 20.5, 41. (c) Corresponding actuation angle plotted against the normalized magnetic flux density. (d) Simulation results for the beams with different aspect ratios under the applied magnetic field $\mathbf{B}^{\mathrm{applied}}$ = 25 mT, which corresponds to the normalized magnetic flux density $G^{-1}\mu_0^{-1}|\tilde{\mathbf{B}}^{\mathrm{r}}||\mathbf{B}^{\mathrm{applied}}| = 0.0094$. The dashed lines indicate the neutral axes of the deformed beams in simulation predictions. (e) Corresponding experimental results with the same dashed lines taken from the simulation results for comparison. Scale bars in (d) and (e) indicate 1 mm.

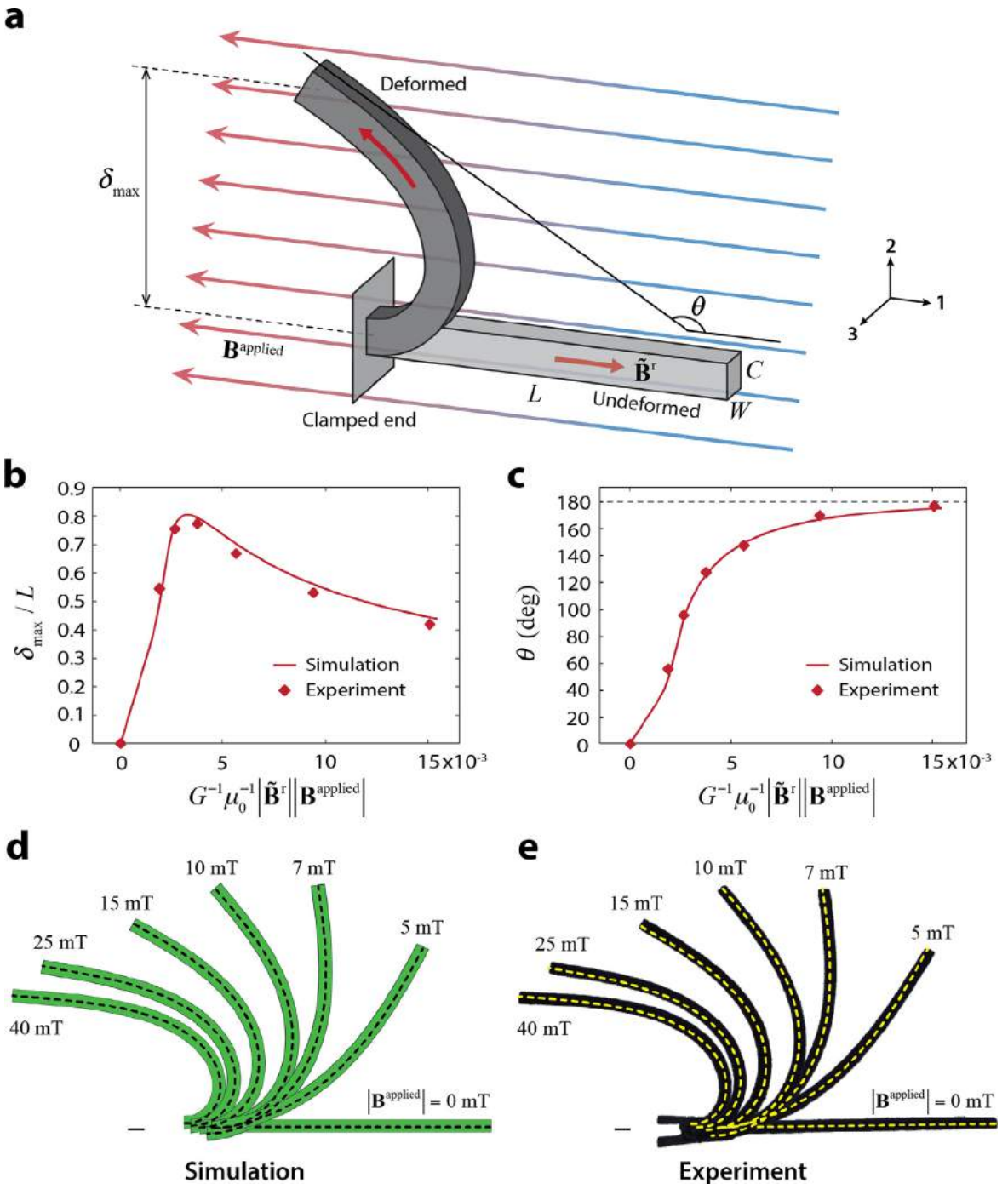

Fig. 8. Validation of the UEL subroutine for extreme bending of a beam up to 180°. (a) Schematic of the actuation of a beam whose initial residual magnetic flux density $\tilde{\mathbf{B}}^r$ is aligned with the 1-direction. During the actuation, one end of the beam is clamped, while the remainder is free to bend under a uniform magnetic field applied in the 2-direction perpendicularly to the beam length. The actuation angle is defined as the angular deviation of the tangent at the tip from the reference length direction. (b) Simulation and experimental results on the relationship between the normalized maximal deflection at the free end, δ_{max}/L, and the normalized magnetic flux density $G^{-1}\mu_0^{-1}|\tilde{\mathbf{B}}^r||\mathbf{B}^{applied}|$ ranging from 0 to 40 mT for beam structures with the same shear modulus G=303 kPa, residual magnetic flux density $|\tilde{\mathbf{B}}^r| = 0.143\,\mathrm{T}(\mu_0^{-1}|\tilde{\mathbf{B}}^r| = 114\,\mathrm{kA/m})$, and aspect ratio $L / C = 20.5$. (c) Corresponding actuation angle plotted against the normalized magnetic flux density. (d) Simulation and experimental results obtained while varying the applied magnetic flux density from 0 to 40 mT. The dashed lines on the simulation results indicate the neutral axes of the deformed beams, which are overlapped with the experimental results for comparison. Scale bars indicate 1 mm.

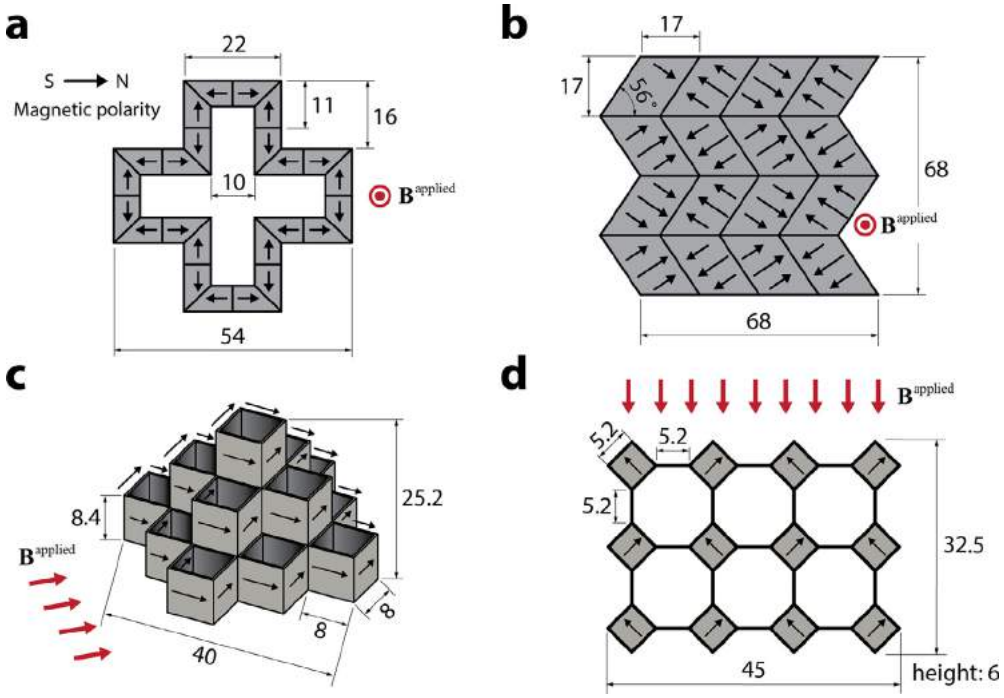

Fig. 9. Schematic design and dimension of selected 2D and 3D structures with programmed magnetic domains (adapted and modified from (Kim et al., 2018)). (a) A hollow cross encoded with alternating patterns of magnetic domains along the perimeter. (b) A Miura-ori fold encoded with alternating oblique patterns of magnetic domains. (c) A pyramid-shaped thin-walled structure programmed to elongate in its diagonal direction along applied magnetic fields. (d) An auxetic structure with a negative Poisson's ratio programmed to shrink in both length and width under applied magnetic fields. The unit for dimensions in this figure is mm.

As can be seen in Fig. 7b and c, our model-based simulation results (solid curves) show good agreement with experimental data (square markers) in terms of both measures: the normalized deflection $\delta_{\max}/L$ and the actuation angle θ. As expected from the analytical model for small bending in Eq. (5.7), beams with higher aspect ratios show larger deflections when compared with beams with lower aspect ratios under the same actuation field $\mathbf{B}^{\text{applied}}$. In addition, the actuation angle θ approaches 90° at lower $\mathbf{B}^{\text{applied}}$ in high-aspect-ratio beams, which implies that, as far as large deflection is concerned, there exists a critical aspect ratio above which the beam reaches the maximum actuation for a given actuation field. As an example, we present the simulation (Fig. 7d) and experimental (Fig. 7e) results for large deflection of a beam with each aspect ratio at a specified actuation field strength $\mathbf{B}^{\text{applied}} = 25$ mT, which corresponds to $G^{-1}\mu_0^{-1}|\tilde{\mathbf{B}}^{\text{r}}||\mathbf{B}^{\text{applied}}| = 0.0094$. These results show that the beam with $L/C = 41$ has reached the maximum actuation at the given condition whereas other beams with smaller aspect ratios have not. For comparison of the simulation and experimental results, the experimental images of the deformed beams in Fig. 7e are overlaid with the dashed lines, each of which indicates the neutral axis of each beam predicted from simulation as indicated in Fig. 7d.

5.5. Extreme bending up to 180°

To create even larger bending up to 180°, the actuation field $\mathbf{B}^{\text{applied}}$ is considered to be applied in reverse to the beam's residual magnetic flux density $\tilde{\mathbf{B}}^{\text{r}}$ as illustrated in Fig. 8a. For simulation and experimental validation of such exterme bending, a beam of $L = 17.2$ mm, $W = 5$ mm, and $C = 0.84$ mm with $L/C = 20.5$ was used with one of its end clamped as previously. The residual magnetic flux density and the shear modulus of the beam were $|\tilde{\mathbf{B}}^{\text{r}}| = 0.143\,\text{T}(\mu_0^{-1}|\tilde{\mathbf{B}}^{\text{r}}| = 114\,\text{kA/m})$ and $G = 303$ kPa, respectively. Similarly to the previous case of large bending up to 90°, the normalized deflection $\delta_{\max}/L$ and the actuation angle θ ($0° \le \theta \le 180°$) were evaluated while varying the applied magnetic flux density from 0 to 40 mT in Fig. 8b and c, which show good agreement between the simulation and experimental results as further validated in Fig. 8d. Again, for better comparison, the experimental images in Fig. 8d were overlaid with the dashed lines which indicate the neutral axes of the deformed beams predicted from the simulation.

6. Model-based simulation of complex 3D shapes

The new fabrication technique to create complex shape-morphing structures based on inscribing intricate patterns of magnetic polarities in 3D-printed soft materials (Kim et al., 2018) in Fig. 2 has necessitated the capability to quantitatively predict such complex transformation by means of model-based simulation. Further extending the scope of validation from

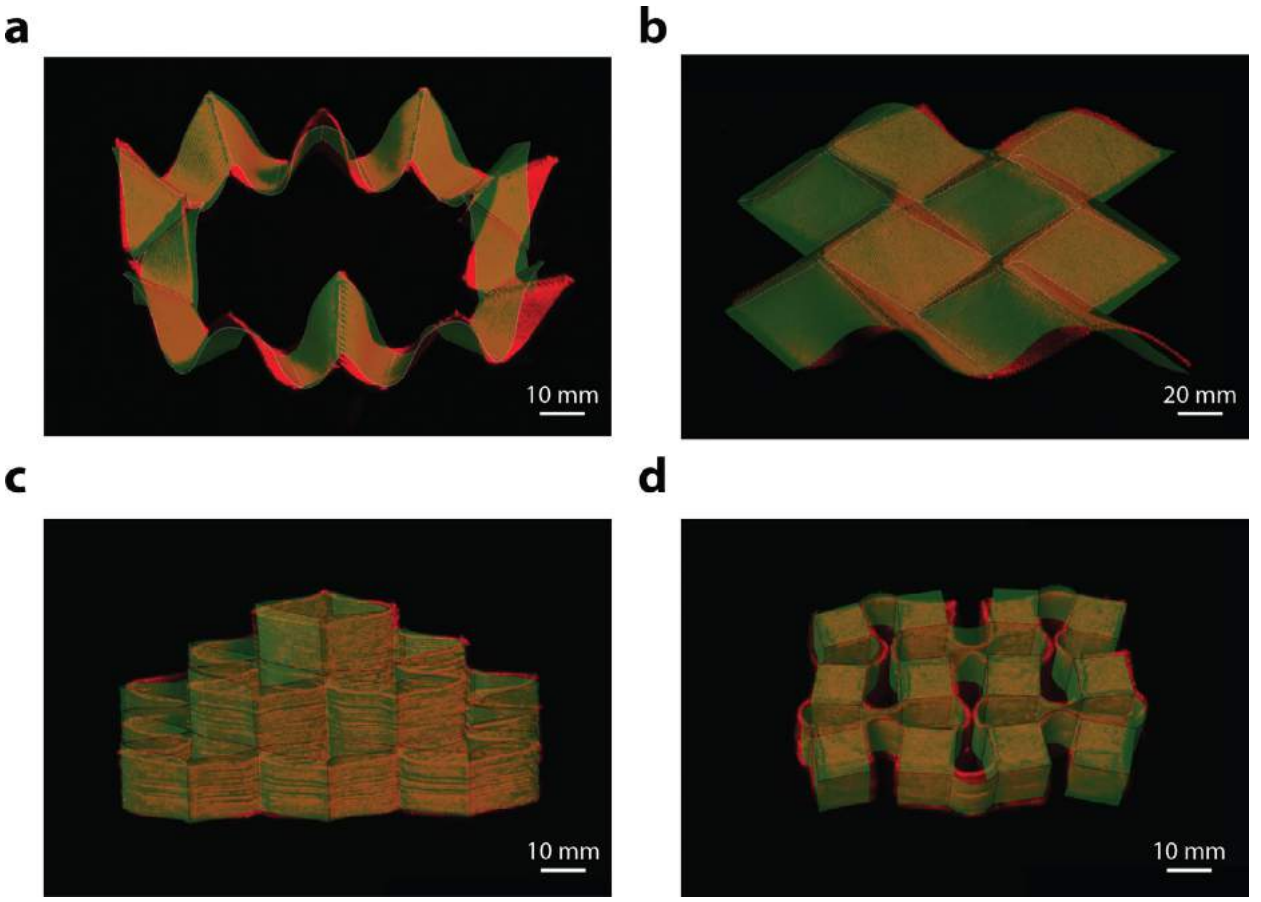

Fig. 10. Experimental images overlaid with finite element simulations of various 2D and 3D structures with programmed magnetic domains presented in Fig. 9. All demonstrated structures were printed with a nozzle of diameter 0.41 mm under a magnetic field generated by a permanent magnet at the nozzle tip. The magnetic actuation was performed by applying external fields of 200 mT generated by a permanent magnet for (a) and (d) and by a pair of electromagnets for (c) and (d) (adapted and modified from (Kim et al., 2018)).

simple bending into such complex transformation, we also compare our model-based simulations with experimental results for a set of printed 2D and 3D structures with programmed shape changes due to the inscribed magnetic domains depicted in Fig. 9. The demonstrated structures were printed with a nozzle with 0.41 mm diameter while applying a magnetic field at the nozzle tip (Kim et al., 2018). The average shear modulus and remanence of the printed structures were $G = 330\,\text{kPa}$ and $|\tilde{\mathbf{B}}^{\text{r}}| = 0.102\,\text{T}(\mu_0{}^{-1}|\tilde{\mathbf{B}}^{\text{r}}| = 81\,\text{kA/m})$, respectively. The magnetic actuation was performed by applying external fields of 200 mT generated by a permanent magnet or a pair of electromagnets perpendicularly to the structures. The observed final shapes under applied magnetic fields are in good agreement with overlaid simulation results as shown in Fig. 10, validating that our model-based simulation can faithfully predict the complex shape changes resulting from the programmed magnetic domains in the demonstrated 3D-printed structures.

7. Conclusions

To quantitatively predict the complex transformation of hard-magnetic soft materials, which has recently been demonstrated in exploratory work (Kim et al., 2018), we have developed a constitutive model for ideal hard-magnetic soft materials based on the framework of isotropic magneto-sensitive Cauchy-elastic solids developed by Dorfmann and Ogden (2003). The ideal hard-magnetic soft material model has been numerically implemented in finite-element analysis. We developed an eight-noded continuum brick element to investigate the magnetically induced deformation in the finite-element software Abaqus/Standard by writing a user-element (UEL). The theory, constitutive model, and numerical implementations have been validated through analytical solutions for homogeneous uniaxial deformation and small-deflection beam bending. A set of experiments have been conducted to verify the constitutive model and numerical implementations for three different cases: small-deflection beam bending, large bending up to 90°, and extreme bending up to 180°.

This work provides an eminently usable and simple theoretical foundation and a robust numerical platform to aid the design of complex structures with programmed magnetic domains for desired functionalities. In addition, the UEL-based

numerical implementation allows multi-physics coupling to be formulated in commercial finite-element program such as Abaqus, which further advances the exploitation of magneto-elastic coupling materials and many other field-responsive materials by accurately predicting their field-actuated deformations. Moreover, such capability to accurately predict the complex shape changes of hard-magnetic soft materials would guide the design of new functional structures and devices for diverse applications such as soft robots and actuators and biomedicine (Hu et al., 2018; Kim et al., 2018). The development of a coarse-grained effective field theory of the considered material system from "first-principles" — perhaps by using principles of homogenization — may be an interesting future endeavor. We remark that the optimal effective media for a magnetically responsive material such as ours may be non-classical (i.e. polar media). However, further experiments are required to see if size-effects are observed or whether a more complex non-classical continua (which admits size-effects) is necessary.

Acknowledgement

This work was supported by National Science Foundation (CMMI-1661627) and Office of Naval Research (N00014-17-1-2920), and the U.S. Army Research Office through the Institute for Soldier Nanotechnologies at MIT (W911NF-13-D-0001). Y.K. acknowledges the financial support through a scholarship from ILJU Academy and Culture Foundation. P.S. acknowledges the financial support from the M.D. Anderson Professorship and the University of Houston. S.A.C. acknowledges the financial support from National Science Foundation (CMMI-1751520 and CMMI-1463121).

References

Arruda, E.M., Boyce, M.C., 1993. A three-dimensional constitutive model for the large stretch behavior of rubber elastic materials. J. Mech. Phys. Solids 41 (2), 389–412.
Bertotti, G., 1998. Hysteresis in Magnetism: for Physicists, Materials Scientists, and Engineers. Academic press.
Bica, I., et al., 2014. Hybrid magnetorheological elastomer: influence of magnetic field and compression pressure on its electrical conductivity. J. Indus. Eng. Chem. 20 (6), 3994–3999.
Borcea, L., Bruno, O., 2001. On the magneto-elastic properties of elastomer–ferromagnet composites. J. Mech. Phys. Solids 49 (12), 2877–2919.
Böse, H., Rabindranath, R., Ehrlich, J., 2012. Soft magnetorheological elastomers as new actuators for valves. J. Intell. Mater. Syst. Struct. 23 (9), 989–994.
Brown, W.F., 1966. Magnetoelastic Interactions. Springer.
Castañeda, P.P., Galipeau, E., 2011. Homogenization-based constitutive models for magnetorheological elastomers at finite strain. J. Mech. Phys. Solids 59 (2), 194–215.
Cezar, C.A., et al., 2014. Biphasic ferrogels for triggered drug and cell delivery. Adv. Healthcare Mater. 3 (11), 1869–1876.
Chester, S.A., Di Leo, C.V., Anand, L., 2015. A finite element implementation of a coupled diffusion-deformation theory for elastomeric gels. Int. J. Solids Struct. 52, 1–18.
Danas, K., Kankanala, S.V., Triantafyllidis, N., 2012. Experiments and modeling of iron-particle-filled magnetorheological elastomers. J. Mech. Phys. Solids 60 (1), 120–138.
de Souza Neto, E., et al., 1996. Design of simple low order finite elements for large strain analysis of nearly incompressible solids. Int. J. Solids Struct. 33 (20–22), 3277–3296.
Deng, H.-x., Gong, X.-l., Wang, L.-h., 2006. Development of an adaptive tuned vibration absorber with magnetorheological elastomer. Smart Mater. Struct. 15 (5), N111.
Dorfmann, A., Ogden, R., 2003. Magnetoelastic modelling of elastomers. Eur. J. Mech. A/Solids 22 (4), 497–507.
Dorfmann, L., Ogden, R.W., 2016. Nonlinear Theory of Electroelastic and Magnetoelastic Interactions. Springer.
Evans, B., et al., 2007. Magnetically actuated nanorod arrays as biomimetic cilia. Nano Lett. 7 (5), 1428–1434.
Evans, B.A., et al., 2012. A highly tunable silicone-based magnetic elastomer with nanoscale homogeneity. J. Magn. Magn. Mater. 324 (4), 501–507.
Fung, Y., 1994. A First Course in Continuum Mechanics: For Physical and Biological Engineers and Scientists. Prentice Hall.
Galipeau, E., Castañeda, P.P., 2013. A finite-strain constitutive model for magnetorheological elastomers: magnetic torques and fiber rotations. J. Mech. Phys. Solids 61 (4), 1065–1090.
Gent, A., 1996. A new constitutive relation for rubber. Rubber Chem. Technol. 69 (1), 59–61.
Ginder, J., 1996. Rheology controlled by magnetic fields. Encyclopedia of Applied Physics 16, 487–503.
Ginder, J., et al., 2002. Magnetostricttve phenomena in magnetorheological elastomers. In: Proceedings of the Electrorheological Fluids and Magnetorheological Suspensions. World Scientific, pp. 472–478.
Ginder, J.M., et al., 1999. Magnetorheological elastomers: properties and applications. In: Proceedings of the Smart Structures and Materials 1999: Smart Materials Technologies 1999. International Society for Optics and Photonics.
Ginder, J.M., Schlotter, W.F., Nichols, M.E., 2001. Magnetorheological elastomers in tunable vibration absorbers. In: Proceedings of the Smart Structures and Materials 2001: Damping and Isolation. International Society for Optics and Photonics.
Harne, R.L., Deng, Z., Dapino, M.J., 2018. Adaptive magnetoelastic metamaterials: A new class of magnetorheological elastomers. J. Intell. Mater. Syst. Struct. 29 (2), 265–278.
Henann, D.L., Chester, S.A., Bertoldi, K., 2013. Modeling of dielectric elastomers: design of actuators and energy harvesting devices. J. Mech. Phys. Solids 61 (10), 2047–2066.
Holzapfel, G.A., 2000. Nonlinear Solid Mechanics: A Continuum Approach for Engineering. Wiley.
Hong, S., et al., 2014. Magnetoactive sponges for dynamic control of microfluidic flow patterns in microphysiological systems. Lab Chip 14 (3), 514–521.
Hu, W., et al., 2018. Small-scale soft-bodied robot with multimodal locomotion. Nature 554 (7690), 81.
Jeong, U.-C., et al., 2013. Magnetorheological elastomer with stiffness-variable characteristics based on induced current applied to differential mount of vehicles. Smart Mater. Struct. 22 (11), 115007.
Jolly, M.R., Carlson, J.D., Munoz, B.C., 1996. A model of the behaviour of magnetorheological materials. Smart Mater. Struct. 5 (5), 607.
Kankanala, S., Triantafyllidis, N., 2004. On finitely strained magnetorheological elastomers. J. Mech. Phys. Solids 52 (12), 2869–2908.
Kashima, S., Miyasaka, F., Hirata, K., 2012. Novel soft actuator using magnetorheological elastomer. IEEE Trans. Magn. 48 (4), 1649–1652.
Kavlicoglu, B., et al., 2011. Magnetorheological elastomer mount for shock and vibration isolation. In: Proceedings of the active and passive smart structures and integrated systems 2011. International Society for Optics and Photonics.
Kim, Y., et al., 2018. Printing ferromagnetic domains for untethered fast-transforming soft materials. Nature 558 (7709), 274–279.
Kovetz, A., 2000. Electromagnetic Theory, 975. Oxford University Press Oxford Vol.
Lai, W.M., et al., 2009. Introduction to Continuum Mechanics. Elsevier Science.
Li, W., et al., 2009. Development of a force sensor working with MR elastomers. In: Proceedings of the IEEE/ASME International Conference onAdvanced Intelligent Mechatronics, 2009, AIM 2009. IEEE.
Li, Y., et al., 2014. A state-of-the-art review on magnetorheological elastomer devices. Smart Mater. Struct. 23 (12), 123001.

Liao, G., et al., 2012. Development of a real-time tunable stiffness and damping vibration isolator based on magnetorheological elastomer. J. Intell. Mater. Syst. Struct. 23 (1), 25–33.
Liu, L., 2014. An energy formulation of continuum magneto-electro-elasticity with applications. J. Mech. Phys. Solids 63, 451–480.
Lum, G.Z., et al., 2016. Shape-programmable magnetic soft matter. Proc. Natl. Acad. Sci. 113 (41), E6007–E6015.
Malvern, L.E., 1969. Introduction to the Mechanics of a Continuous Medium. Prentice-Hall.
McMeeking, R.M., Landis, C.M., 2004. Electrostatic forces and stored energy for deformable dielectric materials. J. Appl. Mech. 72 (4), 581–590.
Nguyen, V.Q., Ramanujan, R., 2010. Novel coiling behavior in magnet-polymer composites. Macromol. Chem. Phys. 211 (6), 618–626.
Ogden, R.W., 1972. Large deformation isotropic elasticity–on the correlation of theory and experiment for incompressible rubberlike solids. Proc. R. Soc. Lond. A 326 (1567), 565–584.
Opie, S., Yim, W., 2011. Design and control of a real-time variable modulus vibration isolator. J. Intell. Mater. Syst. Struct. 22 (2), 113–125.
Pao, Y.-H., 1978. Electromagnetic Forces in Deformable Continua. In: Mechanics today. Volume 4.(A78-35706 14–70) New York, Pergamon Press, Inc., 1978, p. 209–305. NSF-supported research.
Rigbi, Z., Jilken, L., 1983. The response of an elastomer filled with soft ferrite to mechanical and magnetic influences. J. Magn. Magn. Mater. 37 (3), 267–276.
Suo, Z., Zhao, X., Greene, W.H., 2008. A nonlinear field theory of deformable dielectrics. J. Mech. Phys. Solids 56 (2), 467–486.
Tiersten, H., 1965. Variational principle for saturated magnetoelastic insulators. J. Math. Phys. 6 (5), 779–787.
Truesdell, C., Toupin, R., 1960. The Classical Field Theories. Springer.
Wang, S., et al., 2016. Modeling of dielectric viscoelastomers with application to electromechanical instabilities. J. Mech. Phys. Solids 95, 213–229.
Yih-Hsing, P., Chau-Shioung, Y., 1973. A linear theory for soft ferromagnetic elastic solids. Int. J. Eng. Sci. 11 (4), 415–436.
Yin, H., Sun, L., Chen, J., 2006. Magneto-elastic modeling of composites containing chain-structured magnetostrictive particles. J. Mech. Phys. Solids 54 (5), 975–1003.
Zhao, X., et al., 2011. Active scaffolds for on-demand drug and cell delivery. Proc. Natl. Acad. Sci. 108 (1), 67–72.
Zrínyi, M., Barsi, L., Büki, A., 1996. Deformation of ferrogels induced by nonuniform magnetic fields. J. Chem. Phys. 104 (21), 8750–8756.